

# Earth's Future






## RESEARCH ARTICLE

10.1029/2022EF003454

## Frequent but Predictable Droughts in East Africa Driven by a Walker Circulation Intensification

### Special Section:

CMIP6: Trends, Interactions, Evaluation, and Impacts

Chris Funk<sup>1</sup> , Andreas H. Fink<sup>2</sup> , Laura Harrison<sup>1</sup>, Zewdu Segele<sup>3</sup>, Hussen S. Endris<sup>3</sup>, Gideon Galu<sup>1</sup>, Diriba Korecha<sup>1</sup>, and Sharon Nicholson<sup>4</sup> 

<sup>1</sup>Climate Hazards Center, University of California, Santa Barbara, CA, USA, <sup>2</sup>Institute of Meteorology and Climate Research, Karlsruhe Institute of Technology, Karlsruhe, Germany, <sup>3</sup>IGAD Climate Prediction and Applications Center, Ngong, Kenya, <sup>4</sup>Meteorology and Environmental Science, Florida State University, Tallahassee, FL, USA

### Key Points:

- Human-induced warming in the Western V region of the Pacific, combined with La Niña, has produced frequent, predictable March–April–May droughts
- Thermodynamic analyses link these droughts to a stronger Walker Circulation driven by predictable warming in the Western V region
- Projected CMIP6 SST increases imply a tendency for continued Walker Circulation intensification and associated drought risks in eastern East Africa

### Supporting Information:

Supporting Information may be found in the online version of this article.

### Correspondence to:

C. Funk,  
[chris@geog.ucsb.edu](mailto:chris@geog.ucsb.edu)

### Citation:

Funk, C., Fink, A. H., Harrison, L., Segele, Z., Endris, H. S., Galu, G., et al. (2023). Frequent but predictable droughts in East Africa driven by a Walker circulation intensification. *Earth's Future*, 11, e2022EF003454. <https://doi.org/10.1029/2022EF003454>

Received 27 JAN 2023

Accepted 7 OCT 2023

### Author Contributions:

**Conceptualization:** Chris Funk  
**Formal analysis:** Chris Funk, Andreas H. Fink, Laura Harrison, Zewdu Segele  
**Methodology:** Chris Funk, Andreas H. Fink

**Abstract** During and after recent La Niña events, the decline of the eastern East African (EA) March–April–May (MAM) rains has set the stage for life-threatening sequential October–November–December (OND) and MAM droughts. The MAM 2022 drought was the driest on record, preceded by three poor rainy seasons, and followed by widespread starvation. Connecting these dry seasons is an interaction between La Niña and climate change. This interaction provides important opportunities for long-lead prediction and proactive disaster risk management, but needs exploration. Here, for the first time, we use observations, reanalyses, and climate change simulations to show that post-1997 OND La Niña events are robust precursors of: (a) strong MAM “Western V sea surface temperature Gradients” in the Pacific, which (b) help produce large increases in moisture convergence and atmospheric heating near Indonesia, which in turn produce (c) regional shifts in moisture transports and vertical velocities, which (d) help explain the increased frequency of dry EA MAM rainy seasons. We also show that, at 20-year time scales, increases in atmospheric heating in the Indo-Pacific Warm Pool region are attributable to warming Western V SST, which is in turn largely attributable to climate change. As energy builds up in the oceans and atmosphere, during and after La Niña events, we see stronger heating and heat convergence over warm tropical waters near Indonesia. The result of this causal chain is that increased Warm Pool atmospheric heating and moisture convergence sets the stage for dangerous sequential droughts in EA. These factors link EA drying to a stronger Walker Circulation and explain the predictable risks associated with recent La Niña events.

**Plain Language Summary** In 2022, an unprecedented sequence of five sequential failed rainy seasons, exacerbated by high global food and fuel prices, drove an exceptional food security crisis in Ethiopia, Somalia, and Kenya, pushing more than 20 million people into extreme hunger. The potential for famine loomed in some areas. Beginning in late 2020, this was the longest and most severe drought recorded in the Horn of Africa in at least 70 years, resulting in multiple failed harvests and large-scale livestock deaths that decimated the food and income sources of rural communities. It placed increasing pressure on the cost of food among urban communities and led to rising levels of destitution and displacement. These droughts occurred against the backdrop of the “East Africa Climate Paradox”, which centers on the discrepancy between climate change model projections of increased East African March–April–May rains, and many observational studies pointing toward declines. Before the western Pacific Ocean warmed dramatically in 1998, the link between La Niña events and dry March–April–May (MAM) rains was weak. Since 1998, the link has been very strong. This set the stage for dangerous sequential droughts in October–November–December and MAM, such as in 2010/11, 2016/17, 2020/21, and 2021/22. Here, we link the decline to an important question: Why are so many recent La Niña events associated with dry March–April–May rains? La Niña events tend to reach their maximum intensity in the boreal fall and winter, often producing East African droughts during the October–November–December “short rains”. We explain the link between La Niña and dry MAM seasons using observations, reanalyses, and the latest (Phase 6) climate change simulations. While climate change models do not recreate the observed East African drying, they recreate the observed west Pacific warming very well. Climate change, **not** natural decadal variability associated with the Pacific Decadal Oscillation, has increased west Pacific sea surface temperatures. This, in turn, is increasing the “Western V Gradient”, a measure of the east-west differences in Pacific Ocean temperatures. When this gradient is negative, there are frequent East African droughts, and this happens in a predictable way during or after recent La Niña events. This allows us to predict many dry rainy seasons approximately 8 months in advance. Such predictive capacity is important, because the frequency of strong Pacific temperature gradients is increasing. We show that climate change simulations recreate this

© 2023 The Authors. Earth's Future published by Wiley Periodicals LLC on behalf of American Geophysical Union. This is an open access article under the terms of the [Creative Commons Attribution License](https://creativecommons.org/licenses/by/4.0/), which permits use, distribution and reproduction in any medium, provided the original work is properly cited.

**Writing – original draft:** Chris Funk, Andreas H. Fink, Laura Harrison, Zewdu Segele, Hussen S. Endris, Gideon Galu, Diriba Korecha

**Writing – review & editing:** Andreas H. Fink, Laura Harrison, Zewdu Segele, Hussen S. Endris, Gideon Galu, Diriba Korecha

tendency for stronger Pacific SST gradients, and project that it will continue over the coming decades. What connects East African droughts to Pacific temperature gradients? We answer this question by examining observed atmospheric heating, moisture transports, and moisture convergence patterns. In general, eastern East Africa is dry because it resides along the western edge of the Indian Ocean branch of the Indo-Pacific “Walker Circulation”. Across eastern East Africa and the western Indian Ocean, and over the central and eastern Pacific, rainfall and moisture levels are low. In the area around Indonesia (the eastern Indian and western Pacific Oceans), winds drive moisture convergence and heavy rains. Here, building on many years of research by scientists working for the Famine Early Warning Systems Network, we show for the first time that the strength of the Walker Circulation can be quantified using atmospheric heating and moisture convergence. Since 1998, when there has been a La Niña in October–November–December, there has almost always been strong March–April–May heating and moisture convergence around Indonesia, and suppressed rainfall in eastern East Africa. Climate change-enhanced La Niñas amplify the Pacific trade winds which produce strong March–April–May sea surface temperature gradients. These gradients amplify the Walker Circulation, and reduce moisture convergence and ascending atmospheric motions over the eastern Horn of Africa. We conclude with a look toward the future evolution of the Walker Circulation by relating the observed strength of the Walker Circulation to 20-year averages of western and eastern Pacific sea surface temperatures. Both play a significant role, and together explain 96% of the observed variability. The observed Walker Circulation intensification is primarily driven by the west Pacific, which in turn is strongly related to climate change. CMIP6 projections of Pacific sea surface temperatures, combined with the observed empirical relationships, imply further strong increases in Walker Circulation intensities. Hence, additional rainfall declines appear likely, especially during or directly following La Niña events. More optimistically, the process-based analyses presented here suggest that many of the dry seasons may be predictable at long lead times, based on Pacific sea surface temperature gradients.

## 1. Introduction—CMIP6 Simulations Can Enhance Drought Early Warning to Support Food Security

This study examines the drivers of March–April–May (MAM) rains in eastern East Africa (EA), a region of extreme food insecurity and frequent droughts (Shukla et al., 2021). Located near the equator and the descending branch of the Indian Ocean part of the east–west Walker Circulation, this region receives rains in October–November–December (OND) and MAM (Liebmann et al., 2012; Nicholson, 2017). Sequential OND/MAM droughts can have profound food security impacts, such as in 2010/2011, when more 250,000 Somalis perished due to famine (Checchi & Robinson, 2013). In arid eastern East Africa, the MAM “long” rains are relatively short, and intense downwelling radiation, low humidity and very warm air temperatures drive intense atmospheric water demands, which increase further during below-normal rainy seasons (Funk et al., 2021; Funk et al., 2021b). Hence, below normal rainy seasons can be considered “droughts” in the sense that the amount of water provided by rainfall is insufficient to support crops, rangelands, and livestock herds. From 2020 to 2022 an unprecedented sequence of five dry seasons, associated with a 3-year La Niña event, led to a massive humanitarian crisis, potential famine, and widespread loss of livestock and livelihoods (ICPAC et al., 2022a; ICPAC et al., 2022b). These crises occur amidst a continuing and well-documented decline in MAM “long” rains, as first identified by the Famine Early Warning Systems Network (FEWS NET) (Funk et al., 2005; Verdin et al., 2005), and later studies (Lyon, 2014; Lyon & DeWitt 2012; Yang et al., 2014). Following the 1997/98 El Niño, dry MAM seasons became more frequent (Lyon, 2014), while the variability of OND rains increased (Nicholson, 2015). The MAM season is also becoming “shorter not less intense” due to regional circulation changes (Wainwright et al., 2019). Multi-season droughts are particularly dangerous (Nicholson, 2014, 2016). OND–MAM–OND sequential dry seasons are linked to La Niña and warm west Pacific sea surface temperatures (SST) (Anderson et al., 2023). Fortunately, these Pacific SST gradients are very predictable at long leads, and correspondingly offer a foundation for skillful drought forecasts (Funk et al., 2023).

Our focus here is on the potential link between climate change and the dramatic post-1998 increase in the frequency of dry MAM seasons that followed OND La Niñas. This increase sets the stage for dangerous OND/MAM multi-season droughts (Funk et al., 2018), but also opens opportunities for predicting the MAM rains, as in 2017 (Voosen, 2020), 2021, and 2022 (Rubiano, 2022).

During OND, La Niñas are associated with EA dry seasons (Indeje et al., 2000; Ogallo et al., 1988). In the past (between 1950 and 1997), the chance of dry MAM conditions did not increase following OND La Niñas (ICPAC

et al., 2022a). From 1998 to 2022, however, nine dry MAM seasons followed 12 OND La Niña events. This shift, and OND La Niña conditions in 2020, 2021, and 2022, contributed to repetitive droughts and potential famine in EA (ICPAC et al., 2022b). Here, in contrast to other valuable studies that focused on larger domains, regional climate processes, or sub-seasonal drivers (Finney et al., 2020; Nicholson, 2017; Wainwright et al., 2019), we focus on large-scale teleconnections that may help identify, explain, and predict recent below-normal EA MAM rainy seasons. These results help explain regional circulation changes consistent with a “shorter not less intense” rainy season (Wainwright et al., 2019) and the increasing links to the El Niño Southern Oscillation (ENSO) (Park et al., 2020). Our goal is to support early warning and forecasting efforts by explaining the links between La Niña, predictable Pacific SST gradients and EA dry seasons, on both interannual and decadal time-scales.

Our study proceeds in three stages. We first compare CMIP6 simulations to observed EA MAM precipitation and Pacific SST. This links EA drying to human-induced warming in the west Pacific. Then, using reanalyses, we show that strong Pacific SST gradients and Walker Circulation disruptions follow post-1997 La Niñas. Seasons with more intense Walker Circulations are clearly linked to a preponderance of dry EA MAM seasons. Lastly, we use observed Pacific SST gradients and CMIP6 SST projections to suggest that human-induced west Pacific warming has enhanced, and will continue to enhance, the Walker Circulation in ways that are consistent with drying over EA.

### 1.1. Background—Linking the “East Africa Climate Paradox” to La Niña and Walker Circulation Enhancement

Following its introduction in 2015 (Rowell et al., 2015), several papers have discussed the “East African Climate Paradox” (Lyon & Vigaud, 2017; Wainwright et al., 2019). While observations clearly indicate more frequent dry seasons along with later starts and early cessation (Wainwright et al., 2019), climate change simulations have indicated rainfall increases. Although natural Pacific Decadal Variability (PDV) (Lyon, 2014; Lyon & Vigaud, 2017; Yang et al., 2014) might explain this change, it is becoming more and more likely that the “paradox” arises due to the models' systematic biases in SSTs and African circulation features (Lyon, 2020, 2021; Schwarzwald et al., 2022; Shukla et al., 2016; Tierney et al., 2015). The terrain and teleconnections controlling precipitation in EA are complex and poorly resolved by global climate models (Endris et al., 2016). The models tend to misrepresent the mean zonal SST gradients in the Indian Ocean (Lyon, 2021; Lyon & Vigaud 2017; Schwarzwald et al., 2022) and the Pacific Ocean (Seager et al., 2019, 2022). Over EA they tend to have a seasonal cycle that is far too wet in OND and too dry in MAM (Tierney et al., 2013). Multi-model ensembles of regional climate model simulations perform much better (Endris et al., 2013) and indicate future decreases in MAM rainfall (Ogega et al., 2020). Recent evaluations of regional and global climate change models (Endris et al., 2019) indicate stronger future ENSO teleconnections during MAM, consistent with several climate change studies anticipating an increased frequency of strong-gradient La Niñas (Cai et al., 2022; Cai et al., 2015b).

In this study we focus on the relationship between the increased frequency of dry MAM seasons that follow OND La Niñas, and a “Western V Gradient” SST index (WVG) that can support long-lead predictions of EA dry seasons (Funk et al., 2023). The WVG index represents a large-scale Pacific SST pattern where the SST gradients between the central-eastern equatorial Pacific and the western equatorial to extra-tropical Pacific become much stronger than normal, particularly during and following La Niña events. From a food security perspective, the link between OND La Niñas and MAM rainfall deficits is important, because it sets the stage for dangerous sequential droughts (Nicholson, 2014, 2016). Long-lead MAM rainfall forecasts have helped guide humanitarian responses in 2017 (Voosen, 2020), and 2021/2022 (Button, 2022). But while they are effective, there has been relatively little research focused on how strong Pacific SST gradients induce dry EA rainy seasons, why such conditions tend to be associated with La Niña events, and how human-induced warming might be influencing these outcomes.

### 1.2. Definitions

This study is focused on the behavior of the Walker Circulation following recent La Niña events, and how this behavior creates opportunities for prediction. Recent work has discussed the predictability of the MAM rains (Funk et al., 2023). Here, we seek to explain that predictability. Our basic premise is that human-induced warming is interacting with La Niña, producing frequent MAM dry seasons. We begin by using OND NOAA

Oceanic Niño Index (ONI) values (NOAA, 2022) to define La Niña events ( $\text{ONI} < -0.5^{\circ}\text{C}$ ). The strength of human-induced warming can be measured using the “West Pacific Warming Mode” (WPWM), the first empirical orthogonal function of global ENSO-residual SST (Funk & Hoell, 2015). However, the WPWM loads vary strongly in the “Western V” region, a characteristic V-shaped warm SST anomaly pattern that stretches from the area around Indonesia ( $120^{\circ}\text{E}$ – $160^{\circ}\text{E}$ ,  $20^{\circ}\text{N}$ – $15^{\circ}\text{S}$ ) into the northern ( $160^{\circ}\text{E}$ – $150^{\circ}\text{W}$ ,  $20^{\circ}\text{N}$ – $35^{\circ}\text{N}$ ) and southern Pacific ( $155^{\circ}\text{E}$ – $150^{\circ}\text{W}$ ,  $15^{\circ}\text{S}$ – $30^{\circ}\text{S}$ ). Taken together, these three areas correspond to the “Western V region”. Standardized Western V SST time series represent spatial averages across the Western V region. To capture the interaction of warming trends and ENSO, we calculate the WVG, which is a standardized measure of Pacific SST gradients, based on the difference between Niño3.4 ( $170^{\circ}\text{W}$ – $120^{\circ}\text{W}$ ,  $5^{\circ}\text{S}$ – $5^{\circ}\text{N}$ ) and Western V SST time-series. Negative WVG values represent a stronger contrast between the climatologically cool equatorial east Pacific and warm west Pacific. Following rapid Western V warming in 1998 (Funk et al., 2018, 2019), OND La Niñas have been consistently followed by strong negative MAM WVG values. Hence, we describe these 12 MAM seasons (1999, 2000, 2001, 2006, 2008, 2009, 2011, 2012, 2017, 2018, 2021, 2022) as “WVG events”. These events are related to La Niña, but can arise even after a La Niña has faded, because warm Western V SST can still produce La Niña effects (Funk et al., 2018, 2019). Our goals are to better understand links between the WVG and La Niñas, the WVG and the Walker Circulation, and the WVG and climate change. This work has implications for seasonal climate prediction, humanitarian assistance programming, and climate change adaptation (Funk et al., 2023).

## 2. Methods

Our study progresses in three stages, which are described in Sections 2.1, 2.2, and 2.3.

### 2.1. Linking Droughts to Predictable Pacific SST Gradients and Human-Induced Warming in the West Pacific

We begin by evaluating the “East African Climate Paradox” (Rowell et al., 2015) using up-to-date (through 2022) rainfall and SST observations and CMIP6 precipitation simulations. Composites of SSTs for dry and wet seasons are examined. Dry MAM seasons are associated with robust Pacific SST teleconnections, while wet MAM seasons are not. We primarily focus on dry composites, since they, unlike wet events, are associated with coherent SST teleconnections.

Since the west Pacific warmed following the 1997/1998 El Niño (Lyon et al., 2013) and the Walker Circulation intensified (L'Heureux et al., 2013), OND La Niña events (NOAA, 2022) have often been followed by strong negative WVG values in MAM. We investigate the ability of operational seasonal climate models to forecast MAM WVG conditions, using a combination of hindcasts and forecasts from the preceding September. We show that these WVG predictions do a good job of identifying many dry MAM seasons at long leads. Then, using CMIP6 simulations, we examine the level of correspondence between the simulated SST warming trends, observed outcomes in the Niño 3.4 and Western V regions, and the WVG.

### 2.2. Linking La Niña/WVG Events to Walker Circulation Intensification

This section examines interannual WVG influences on MAM Indo-Pacific atmospheric heating, moisture transports, and moisture convergence fields. Long term means and WVG anomalies in atmospheric heating and moisture transports can be used to explore the Indian and Pacific branches of the Walker Circulation (Bjerknes, 1969). Note that we use the term “Walker Circulation” to broadly refer to the complex Indo-Pacific circulation patterns linking the Pacific to the Warm Pool region near Indonesia, and the Warm Pool region to MAM EA rains. While we present equatorial longitude-by-height results, we also examine spatial maps that emphasize how extra-tropical SST and atmospheric heating gradients act to modulate moisture transports.

Our thermodynamic approach was inspired by studies using vertically integrated transports of heat energy (internal energy,  $T$ ) and geopotential height energy (potential energy,  $Z$ ) (Peixoto & Oort, 1992; Trenberth & Stepaniak, 2003a, 2003b).  $T$  is a function of the vertical temperature distribution and specific heat capacity of air.  $Z$  is a function of geopotential height and the acceleration due to gravity ( $g$ ). These are the two largest atmospheric energy terms. In atmospheric thermodynamics, it is common to combine these two terms to describe Dry Static Energy (DSE):

$$\text{DSE} = T + Z \quad (1)$$

DSE is a conserved quantity. Changes in DSE, however, arise from the introduction of external heating, commonly referred to as diabatic heating. Latent heating (LH) due to precipitation, radiation (R), and sensible heating (SH) in the planetary boundary layer are the largest sources of diabatic heating. The R term here is a measure of the net radiation into a column of air, that is, a combination of the downward and upward shortwave and longwave radiation from the top of the atmosphere and surface of the Earth. Increased atmospheric water vapor contributes to increased trapped longwave radiation and increased precipitation. As the atmosphere warms and saturation vapor pressures increase, these heating terms are likely to increase as well. The modulation of DSE by external (diabatic) heating leads to:

$$\text{diabatic heating} = \text{Div}(T) + \text{Div}(Z) \quad (2)$$

Div(T) and Div(Z) are vertically-integrated divergence terms, based on vertically integrated temperature and geopotential height fluxes. While accurate, the standard DSE formulation of these terms obscures the fact that Div(T) and Div(Z) are strongly anti-correlated, due to hydrostatic relationships (Peixoto & Oort, 1992). Converging heat in the lower and middle troposphere (i.e., Con(T)) causes a column of air to stretch, raising upper-level heights, and increasing Div(Z). In rainy areas of the Walker Circulation, heat converges in the lower troposphere, and geopotential height energy diverges aloft. Persistent heating in the Indo-Pacific Warm Pool area produces equatorially-trapped Rossby and Kelvin waves, which (respectively) help establish the Indian and Pacific branches of the Walker Circulation (Gill, 1980, 1982). To measure the strength of this forcing, we combine diabatic heating and heat convergence into a single “atmospheric heating” term, measured in  $\text{Wm}^{-2}$ .

$$\text{atmospheric heating} = \text{Con}(T) + \text{diabatic heating} \quad (3)$$

As we will show, this framework provides a useful description of the humid and dry regions of the Walker Circulation. Areas with low level convergent winds will have both heat convergence Con(T) and moisture convergence Con(Q). Direct heating by heat convergence will be augmented by the latent heat released via precipitation, since moisture is also conserved:

$$\text{precipitation} = \text{Con}(Q) - \text{evaporation} \quad (4)$$

Because evaporation in Warm Pool areas tends to be low, precipitation  $\approx$  Con(Q). More moisture will also increase the trapping of longwave radiation. Equation 3, therefore, stacks covarying heating terms. From first principles, a warming atmosphere might experience increased heat convergence, simply due to increases in air temperatures. Warmer air also holds more water vapor, leading to increases in precipitation and decreases in outgoing longwave radiation. This logic also supports combining the Con(T) and diabatic heating terms. We examine these variables to formally evaluate whether WVG events and Walker Circulation enhancement are linked to dry EA rainy seasons and changes in the Indian Ocean branch of the Walker Circulation.

### 2.3. Linking Western V Warming to Walker Circulation Intensification and More Frequent Dry EA Rainy Seasons

Our final analysis focuses on decadal changes in the strength of the Walker Circulation and the frequency of below-normal MAM rainy seasons. We begin by updating the observational West Pacific Warming Mode (WPWM) analysis from Funk and Hoell (2015). This Empirical Orthogonal Function analysis underscores the points that (a) Niño 3.4 and Western V SSTs closely track the first two modes of global SST, and (b) the climate change-related WPWM, along with Western V SSTs, continues to increase rapidly. We then use regression to link 20-year average Western V and Niño 3.4 SST to 20-year averages of Warm Pool atmospheric heating. We show that these SST values explain very well 20-year changes in Warm Pool atmospheric heating and that the Western V warming has played an important role in the recent Walker Circulation intensification and the increased frequency of dry East African rainy seasons. CMIP6 SST ensembles are used to estimate increases in Warm Pool heating through 2050.

## 3. Data

Dry and wet seasons are defined using Climate Hazards InfraRed Precipitation with Stations (CHIRPS) (Funk et al., 2015) satellite-gauge and Centennial Trends (Funk et al., 2015) interpolated gauge datasets. These widely

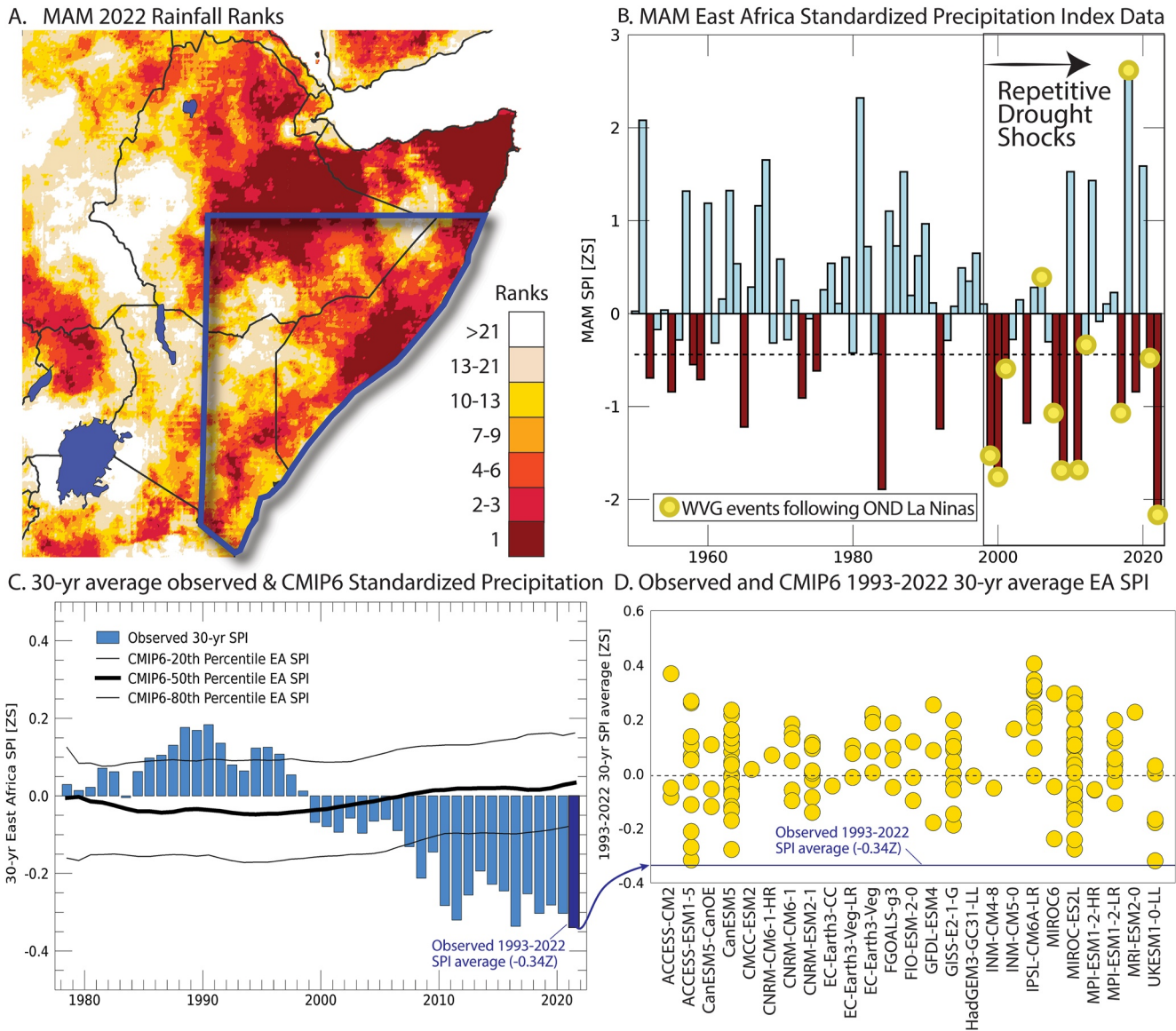


**Figure 1.** Describing the East African Climate Paradox. (a) MAM 2022 rainfall ranks indicate most of the Horn of Africa received extremely low rainfall amounts, based on 42 years of CHIRPS rainfall. The blue polygon denotes the Eastern East Africa (EA) region. (b) Time-series of dry region MAM CHIRPS/Centennial Trends rainfall, expressed as Standardized Precipitation Index (SPI) values). Yellow circles identify MAM WVG events. (c) Observed (blue bars) and simulated CMIP6 SSP245 30-year average EA SPI. Centered on a 1981–2021 baseline. Based on 152 CMIP6 simulations. The thick and thin black lines show the median and 20th/80th quantiles of the CMIP6 simulation distribution. (d) The 152 simulated CMIP6 1993–2022 30-year average East Africa SPI, centered on a 1981–2021 baseline. The horizontal line in (d) denotes the observed 1993–2022 average EA SPI value (−0.34Z).

used data sets were specifically developed to work well in East Africa, have been shown to work well (Dinku et al., 2018), and incorporate many additional rain gauge observations provided by collaborators at Florida State University (Nicholson, 2017), the Ethiopia National Meteorological Agency (~120 stations), and the Somali Food Security and Nutrition Analysis Unit (~90 stations).

The EA area of focus (Figure 1a) is based on a homogeneous rainfall area—Ethiopia, Somalia and Kenya east and south of 38°E and 8°N. This food insecure region (Shukla et al., 2021), has been the center of focus for several previous studies (Funk et al., 2014, 2018, 2019; Liebmann et al., 2014). Unlike other studies that examine a broader area (Finney et al., 2020; Walker et al., 2020), we focus on this extremely food insecure region (Shukla et al., 2021) because of its recent tendency for frequent sequential droughts, especially during or following recent La Niña events (Funk et al., 2014; Funk et al., 2018; Funk et al., 2019; Hoell & Funk 2013a, 2013b; Liebmann et al., 2014; Williams & Funk, 2011).

**Table 1**  
*The CMIP6 SSP245 Models and Simulations Used in This Study*

Model names	Number of simulations
ACCESS-CM2	3
ACCESS-ESM1-5	11
CanESM5-CanOE	3
CanESM5	25
CMCC-ESM2	1
CNRM-CM6-1-HR	1
CNRM-CM6-1	6
CNRM-ESM2-1	9
EC-Earth3-CC	1
EC-Earth3-Veg-LR	3
EC-Earth3-Veg	5
FGOALS-g3	4
FIO-ESM-2-0	3
GFDL-ESM4	3
GISS-E2-1-G	10
HadGEM3-GC31-LL	1
INM-CM4-8	1
INM-CM5-0	1
IPSL-CM6A-LR	11
MIROC6	3
MIROC-ES2L	30
MPI-ESM1-2-HR	2
MPI-ESM1-2-LR	9
MRI-ESM2-0	1
UKESM1-0-LL	5
Total Number of Sims	152

Areal averages of the 1981–2022 EA CHIRPS and the 1900–2014 Centennial Trends correlate very well over their period of overlap (1981–2014). A bivariate regression is used to transform Centennial Trends values into CHIRPS-compatible regional averages over the 1950–1980 period. A Gamma distribution fit is then used to develop a Standardized Precipitation Index (SPI) times-series (Husak et al., 2007). This time series, and all other analyses in this study, are centered on a 1981–2021 baseline. Dry and wet seasons will be based on the EA SPI values below and above  $-0.44Z$  and  $+0.44Z$ , which corresponds with a 1-in-3 years low or high value. Dry seasons may occasionally be described as droughts, to avoid repetition.

Version five of the NOAA Extended Reconstructed SST (Huang et al., 2017) is used to represent observed ocean temperatures. To explore circulation changes we use ERA5 (Hersbach et al., 2020) and MERRA2 (Gelaro et al., 2017) reanalyses. Our analysis looks at moisture transports and the combined influence of local diabatic heating and atmospheric heat convergence. We also include in our study September forecasts of MAM SSTs from the North American Multi-Model Ensemble (NMME) (Kirtman et al., 2014). Our study also uses a multi-model ensemble of 152 Shared Socio-Economic Pathway 245 SST simulations from the latest CMIP version 6 (CMIP6) archive (Eyring et al., 2016) (Table 1). The moderate SSP245 scenario is based on projections of large increases in sustainable development and  $4.5 \text{ Wm}^{-2}$  of radiative forcing by 2100 (Meinshausen et al., 2020). CMIP6 data were accessed from Lawrence Livermore National Laboratory (LLNL) node of the Earth System Grid Federation (ESGF) platform (<https://esgf-node.llnl.gov/search/cmip6/>).

Finally, it should be noted that most of our observational results focus on the 1981–2022 time period, during which satellite data informs our precipitation estimates and reanalyses. While we do present longer time-series of EA rainfall, and changes in 1950–2022 ERA5 WVG events, the bulk of our analysis focuses on the past 42 years. This allows for cross-checks between the ERA5 and MERRA2 reanalyses. The MERRA2 results were very similar, and hence have been omitted in our figure set. Confirmatory time series scatterplots based on the MERRA2 reanalysis are available in the accompanying supporting data set.

## 4. Results and Discussion

### 4.1. Links Between OND La Niña, Predictable Strong Western V Gradients and EA Droughts

In MAM 2022, rains in Ethiopia, Kenya and Somalia were exceptionally poor (Figures 1a and 1b). Since 1999, 11 MAM EA seasons have been dry. Many of these dry seasons followed the 12 post-1997 OND La Niñas (yellow circles, Figure 1b). La Niña conditions (as defined by the ONI) continued into MAM during many of these events (8 of 12). A consistent feature that appears to dynamically relate to EA MAM dry seasons (Funk et al., 2018, 2019) is that even when the La Niña conditions have faded, strong Pacific SST gradients, augmented by west Pacific warming, have persisted. This is explored further below.

#### 4.1.1. CMIP6 Representation of Observed EA Drying

The observed drying tendency in EA MAM Standardized Precipitation Index (SPI) values (blue bars/line in Figures 1c and 1d) contrasts with historical climate change model simulations (Table 1) for this region (black line/yellow circles in Figures 1c and 1d). Since 1999, frequent (11) dry seasons have suppressed the 30-year average SPI, resulting a mean 1993–2022 SPI value of  $-0.34Z$ . Time-series of 30-year average SPI values from 152 CMIP6 SSP245 simulations indicate little change in EA MAM precipitation. The last observed and simulated values from these time-series (1993–2022 average SPI) are expanded in Figure 1d, which breaks the results out by model. The distribution of per-model CMIP6 SPI values for the recent period sits firmly higher than the

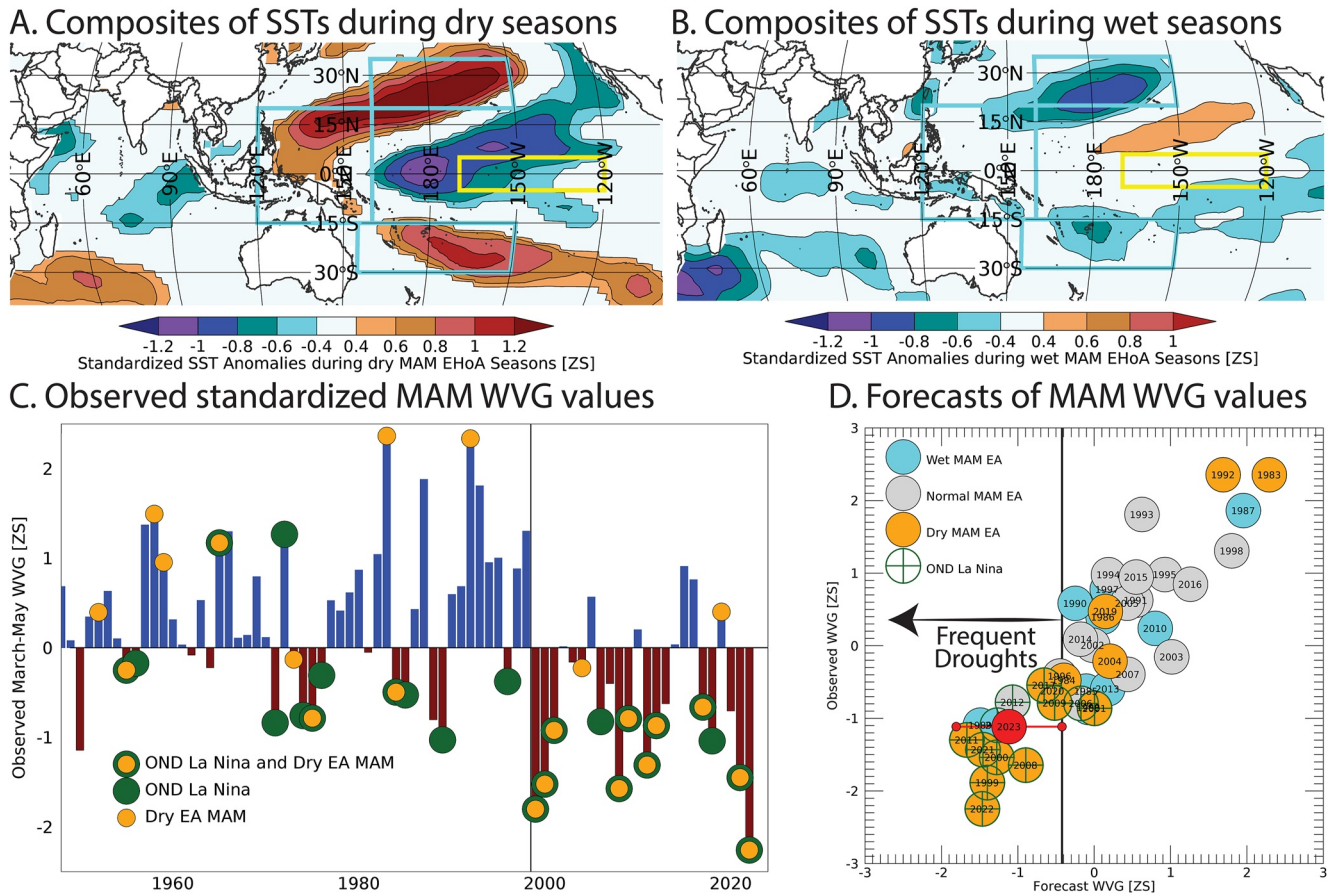


**Figure 2.** Relating dry seasons to the Western V Gradient. (a) and (b) Composites of standardized SSTs during 1981–2022 dry seasons (a) and wet seasons (b) reveal a substantial non-linearity. Dry seasons exhibit a coherent dipole pattern in the Pacific, while wet seasons SST anomalies exhibit few areas with significant relationships. Wet and dry seasons based on 1981–2022 EA SPI values of greater than +0.44 or less than –0.44. These breaks correspond with the top and bottom tercile boundaries. Screened for significance at  $p < 0.1$  using a two-tailed  $t$ -test. The cyan boxes in A and B denote the equatorial [120–160°E, 20°N–15°S], northern [160°E–150°W, 20–35°N], and southern [155°E–150°W, 15–30°S] regions of the “Western V” area. The yellow box denotes the Niño 3.4 region in the eastern equatorial Pacific [170–120°W, 5°N–5°S]. The WVG is the standardized difference between the Niño 3.4 and Western V areas. (c) A bar plot of observed standardized MAM WVG values, centered on a 1981–2021 baseline. Orange circles denote dry EA MAM seasons. Green circles denote preceding OND La Niña years. Orange within green circles identify OND La Niña seasons followed by dry EA MAM events. The thin vertical line at between 1998 and 1999 identifies the shift toward stronger WVG values and more frequent dry EA MAM rainy seasons. (d) Scatterplot showing forecasts of MAM WVG index values, based on September NMME SST predictions. Observed MAM EA rainy season outcomes shown with blue/gray/orange shading. All time-series and SST are centered on a 1981–2021 baseline. Also shown are preceding OND La Niña seasons (green crosses), and the 2023 WVG forecasts (in red). The  $y$ -axis value has been set to the forecast value. 80% confidence intervals for the forecast are also shown with small red circles and a horizontal red line.

observed value of  $-0.34Z$ . This discrepancy is important. The models' precipitation simulations are likely being skewed by some combination of model deficiencies. For example, the climate change models do not capture Indian Ocean zonal SST gradients well (Schwarzwalder et al., 2022), which impacts their ability to recreate the seasonal cycle and the Indian Ocean branch of the Walker Circulation. They also exhibit Pacific zonal SST biases, which may account for their inability to recreate the observed strengthening of the Walker Circulation (Seager et al., 2019, 2022). Finally, they recreate observed teleconnection patterns and climatological seasonal cycles poorly (Endris et al., 2016, 2019, 2021).

#### 4.1.2. EA Drought Connections to ENSO Events and Western V Warming

Composites of standardized MAM SSTs during 1981–2022 dry EA seasons (Figure 2a) exhibit a contrast between a warm “Western V” region in the west Pacific and cool central-east Pacific SSTs; that is, a negative WVG SST pattern. Interestingly, while dry MAM season composites exhibit significant links to the Pacific (Figure 2a), and some relation to Indian Ocean SSTs, wet season composites indicate less strong links (Figure 2b). Non-linearities have been previously identified for the OND season (Nicholson, 2015), but have received little attention in



**Table 2**  
CPC ONI Values Along With Standardized Western V, Niño3.4 and WVG Values for MAM Seasons Following Recent Strong El Niño Events

El Niño event	MAM	MAM ONI	MAM western V	MAM WVG	MAM ERA5 Warm pool heating
1972/73	1974	-1.0 C	-0.9Z	-0.8Z	418 Wm <sup>-2</sup>
	1975	-0.7 C	-0.3Z	-0.8Z	521 Wm <sup>-2</sup>
1982/83	1984	-0.4 C	-0.1Z	-0.5Z	442 Wm <sup>-2</sup>
	1985	-0.8 C	-0.7Z	-0.5Z	420 Wm <sup>-2</sup>
Four MAM average		-0.7	-0.5Z	-0.7Z	450 Wm <sup>-2</sup>
1997/98	1999	-1.0 C	+1.3Z	-1.8Z	578 Wm <sup>-2</sup>
	2000	-0.8 C	+1.1Z	-1.5Z	556 Wm <sup>-2</sup>
2015/16	2017	+0.2 C	+1.5Z	-0.7Z	532 Wm <sup>-2</sup>
	2018	-0.5 C	+1.0Z	-1.0Z	376 Wm <sup>-2</sup>
Four MAM average		-0.6 C	+1.2Z	-1.3Z	510 Wm <sup>-2</sup>

Note. Also shown are the associated MAM ERA5 Warm Pool atmospheric heating values.

MAM. For OND, canonical ENSO forcing on EA appears to be mediated via strong relationships with the Indian Ocean Dipole (MacLeod et al., 2021). The composites shown in Figures 2a and 2b suggest that dry MAM seasons may be more predictable than wet seasons, based on much more coherent large-scale SST patterns.

There has been a marked increase in the frequency of strong negative WVG conditions since the late 1990s during MAM. These have primarily followed recent OND La Niñas and are also associated with many of the recent dry EA MAM seasons (Figure 2c). For the 12 OND La Niñas since 1998, MAM WVG values the following year ranged from -0.8Z to -2.2Z. Nine of these EA MAM seasons were dry. The increased frequency of strong negative WVG are associated with strong warming trends in the western Pacific (Funk et al., 2018, 2019) and frequent La Niñas during this time.

While post-1997 warming has increased the sensitivity of EA MAM rains to the Western V region, it is also important to recognize the risks associated with Walker Circulation enhancements following strong El Niño events. A strong El Niño, followed by La Niña and warm West Pacific SST, can set the stage for sequential droughts across eastern and southern Africa (Funk et al., 2018). Here, we briefly explore MAM ONI, WVG and Warm Pool atmospheric heating values during the 2 years that followed the strongest El Niño events over the past 50 years: The 1972/1973, 1982/1983, 1997/1998,

and 2015/2016 El Niño events. These had boreal winter ONI values exceeding +2°C. La Niña conditions were present during most of these MAM seasons (six of the eight), based on MAM ONI values of less than -0.5 C. While the small sample size limits confidence, there are notable differences in SST and Warm Pool atmospheric heating that suggest substantially greater La Niña drought risks following the more recent (post-1997) strong El Niño events, associated with a stronger Walker Circulation. The MAM seasons after these events have a combination of warmer Western V SSTs (+1.2Z vs. +0.5Z), stronger negative WVG values (-1.3Z vs. -0.7Z), and higher Warm Pool atmospheric heating values (~510 Wm<sup>-2</sup> vs. 450 Wm<sup>-2</sup>) (Table 2). This is consistent with the idea that climate change contributes to hazards by increasing the chance of both exceptionally warm Niño 3.4 and Western Pacific SSTs (Funk et al., 2018). A logistic regression linking heating to the probability of a dry EA season (see Section 4.4 below), associates this change in heating with a shift in the probability of a dry MAM EA season from about 45% to 65%. Taken together, these results suggest that strong El Niño events may help trigger multi-year La Niña events, and that the risks of dry EA MAM seasons during these events will likely be increased due to anthropogenic Western V Warming and associated Walker Circulation enhancements.

#### 4.1.3. Opportunities and Challenges for Seasonal Drought Prediction

We can predict WVG conditions at long leads, allowing us to predict many of the events that produce the decline in EA rains. As an example, Figure 2d shows forecasts of MAM WVG values, based on September North American Multi-Model Ensemble climate forecasts (Kirtman et al., 2014). MAM Western V, WVG and Niño 3.4 SSTs are all predicted very well by the NMME (1982–2022 R<sup>2</sup> 0.77, 0.77, 0.67). When WVG values are predicted to be negative (<-0.5Z) we see a preponderance of dry EA MAM rainy seasons, and many of the seasons with low WVG values follow OND La Niñas. The fact that long-lead WVG forecasts (Figure 2d) successfully discriminate many drought events is very important, because this result implies that we can anticipate dangerous OND/MAM sequential droughts, which in 2020–2022 brought five sequential dry seasons and the threat of starvation to millions in Ethiopia, Kenya, and Somalia (ICPAC et al., 2022a).

While the potential predictability of the WVG and associated dry MAM seasons is promising, it is also important to recognize the important influence of sub-seasonal climate variations, such as those associated with the Madden-Julian Oscillation (MJO). The MJO is the dominant source of sub-seasonal climate variability in the tropics (Zhang, 2005). The MJO is known to strongly modulate MAM rains in East Africa (Maybee et al., 2022; Pohl & Camberlin, 2006). The eastward propagation of the MJO can be quantified using two indices, based on the empirical orthogonal function (EOF) of three variables: 200 and 850 hPa equatorial zonal winds and outgoing longwave radiation (Wheeler & Hendon, 2004). Together, these two EOFs form the Realtime Multi-variate MJO indices (RMM1 and RMM2). Daily MAM RMM indices, obtained from the Australian Bureau of Meteorology

**Table 3**  
*Standardized MAM Niño3.4, Western V, and WVG NMME SST Forecasts for Sequential Months Between October 2022 and April 2023*

Forecast date	Niño3.4	Western V	WVG
Early October 2022	−0.2Z	+2.5Z	−1.1Z
Early November 2022	−0.1Z	+2.6Z	−1.1Z
Early December 2023	−0.1Z	+2.5Z	−1.0Z
Early January 2023	−0.1Z	+2.4Z	−0.9Z
Early February 2023	−0.2Z	+2.4Z	−1.0Z
Early March 2023	0.0Z	+2.0Z	−0.6Z
Early April 2023	+0.8Z	+2.1Z	−0.3Z

are shown for 2018 and 2023 in Figure S1 in Supporting Information S1. The various regions of deep convection (or “phases”) are identified with values from 1 to 8. As discussed by Maybee et al. (2022), phases 1-to-4 are associated with enhanced East African MAM rainfall. In 2018, as discussed in Kilavi et al. (2018), MJO activity in phases 2, 3, and 4 combined with shorter term influences associated with tropical cyclones over the southwestern Indian Ocean to drive “an anomalous westerly low-level circulation over Kenya and the surrounding region”, supporting enhanced moisture convergence and extreme rains. Through mid-May 2023 MJO index values also indicate enhanced MJO activity in March, April and early May (Figure S1b in Supporting Information S1). While detailed analyses of the sub-seasonal variations are beyond the scope of this study, wet MAM seasons in 2018 and 2023 are important reminders of the limits of seasonal climate predictability.

In addition to sub-seasonal influences, in 2023 the Pacific climate system also transitioned rapidly from La Niña to El Niño conditions. This transition was captured well by the NMME forecasts (Table 3, Figure S2 in Supporting Information S1). Between late 2022 and February of 2023, monthly updates of the NMME model forecasts for MAM presented a very consistent outlook: neutral Niño 3.4 conditions paired with exceptionally warm Western V values, resulting in MAM WVG predictions ranging from −0.9 Z to −1.1 Z. These conditions were similar to the MAM 2017 dry season, as in these were concerning but not as extreme as predictions for seasons like 1999 or 2022, which also anticipated cool Niño 3.4 conditions. Forecasts for MAM from early March changed substantially. Predicted MAM Niño 3.4 SSTs warmed while MAM Western V forecasts cooled, resulting in a weak WVG forecast of −0.6Z. By the following month, the NMME forecast MAM Niño3.4 SST climbed to +0.8Z, and the WVG outlook dropped to −0.3 Z. Thus, WVG forecasts can capture rapid shifts in ENSO, though these rapid transitions will not always be captured well by long-lead predictions. During multi-year La Niña sequences, a three-season OND-MAM-OND EA dry sequence is common, while the link to the second MAM season (i.e., OND-MAM-OND-MAM) is weak (Anderson et al., 2023).

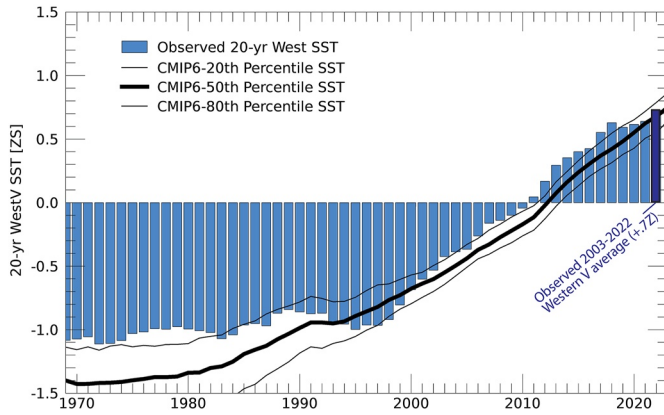
#### 4.1.4. CMIP6 Representation of Observed SST Trends

Figure 3 presents observed and simulated changes in 20-year MAM Western V, Niño 3.4 and WVG time-series. For the Western V, the observations track very closely with the CMIP6 simulations (Figure 3a). The correlation between the CMIP6 median Western V values and the observed Western V time-series is 0.96. The CMIP6 simulations suggest that climate change, not natural Pacific Decadal variability, has resulted in large SST increases in the Western V region. The pace of observed warming has increased dramatically over the past 20 years. The observed 2003–2022 Western V average falls comfortably within the CMIP6 distribution (Figure 3b).

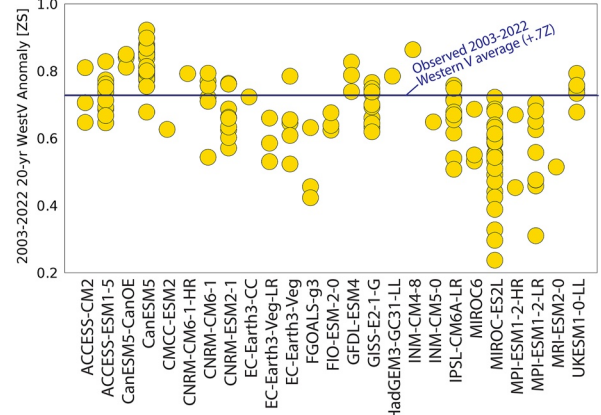
The Western V warming contrasts with Niño 3.4 outcomes (Figures 3c and 3d). As noted by other studies, in observations, there is marked lack of warming in the eastern Pacific (Seager et al., 2019, 2022). The CMIP6 ensemble, on the other hand, simulates substantial warming. The median of the CMIP6 simulations (heavy black line in Figure 3c) increases from −0.5 C to +0.3 C. The individual CMIP6 simulation Niño 3.4 results are shown in Figure 3d. The 2003–2022 mean values range from −0.1Z to +0.7Z. Given that each simulation represents an independent simulation, these results will be driven by some combination of natural decadal variability, climate change, and potential model bias. Given that 151 out of 152 Niño 3.4 simulations are warmer or much warmer than the observed 2003–2022 mean (−0.1Z), it appears unlikely that the observed lack of warming has arisen solely through natural decadal variability. Rather, it seems increasingly likely that systematic biases in Pacific SST may also be contributing to this discrepancy (Seager et al., 2019, 2022).

Since the CMIP6 simulations recreate the observed Western V warming (Figures 3a and 3b), but overestimate the Niño 3.4 warming (Figures 3c and 3d), the CMIP6 WVG trends suggest a strengthening of the WVG that is weaker than the strengthening of the gradient in the observations (Figures 3e and 3f). Nevertheless, they anticipate more negative WVG values. If the CMIP6 models are over-estimating warming in the Niño 3.4 region, then climate change would account for a greater portion of the observed decrease in WVG values.

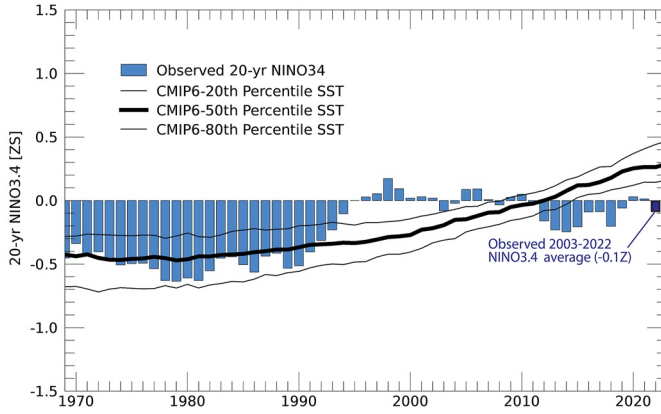
A. Observed & CMIP6 20-yr Western V SST anomalies



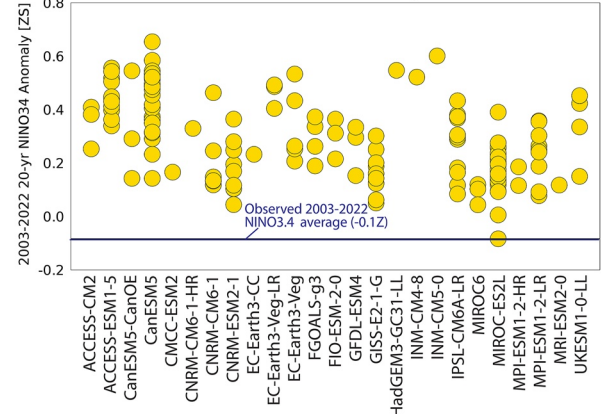
B. Individual CMIP6 2003-2022 20-yr Western V SST



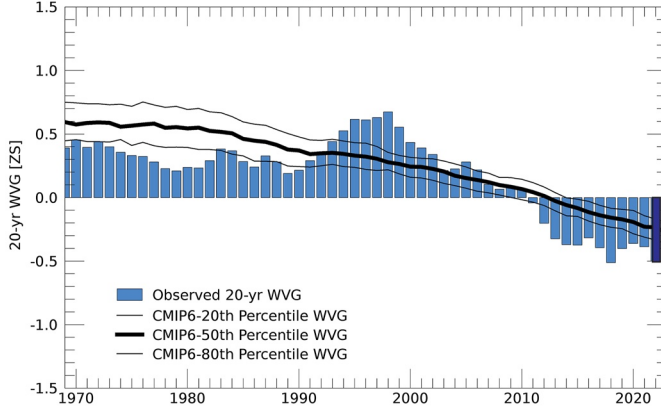
C. Observed & CMIP6 20-yr Nino3.4 SST anomalies



D. Individual CMIP6 2003-2022 20-yr Niño3.4 SST



E. Observed & CMIP6 20-yr WVG values



F. Individual CMIP6 2003-2022 20-yr WVG values

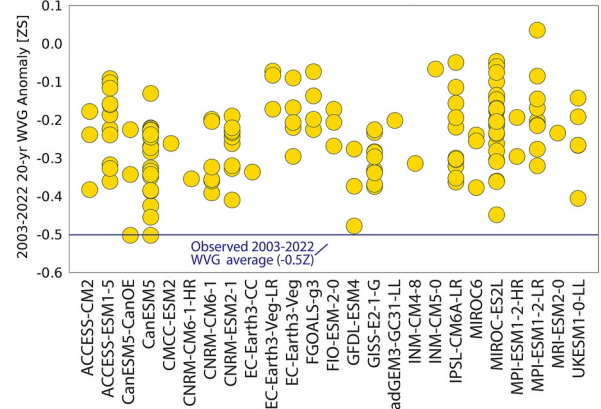
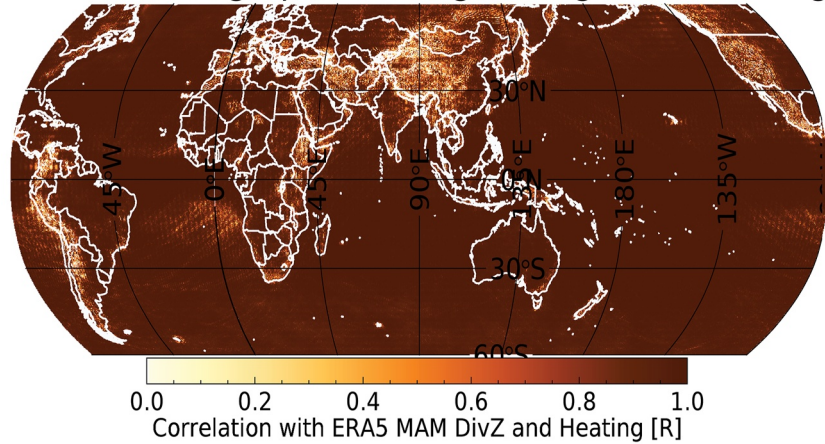


**Figure 3.** Observed and CMIP6 SST time-series. (a) Observed (blue bars) and CMIP6 SSP245 projections of 20-year averages of standardized Western V SST anomalies. Centered on a 1981–2021 baseline. CMIP6 results based on 152 CMIP6 simulations. The thick and thin red lines show the median and 20th/80th quantiles of the CMIP6 simulation distribution. (b) Individual CMIP6 simulated 2003–2022 20-year average Western V SST anomalies, centered on a 1981–2021 baseline. The horizontal line in (b) denotes the observed average 2003–2022 standardized Western V SST anomaly (+0.7Z). (c) and (d). Same but for standardized Niño 3.4 SST anomalies. (e) and (f). Same but for standardized WVG index values.

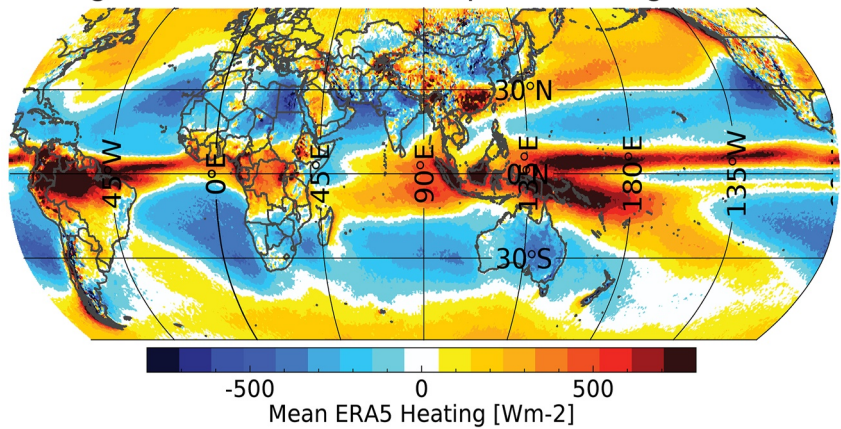
4.2. Linking WVG Events to Large and Energetic Changes in the Walker Circulation

A better understanding of the processes that link Pacific SSTs and dry EA outcomes will help build confidence in dry season predictions, which will make them more actionable. To that end we examine MAM WVG circulation anomalies using ERA5 reanalyses.

A. Correlation of geopotential height divergence and heating



B. Long term mean of ERA5 atmospheric heating



C. Long term mean of geopotential height convergence

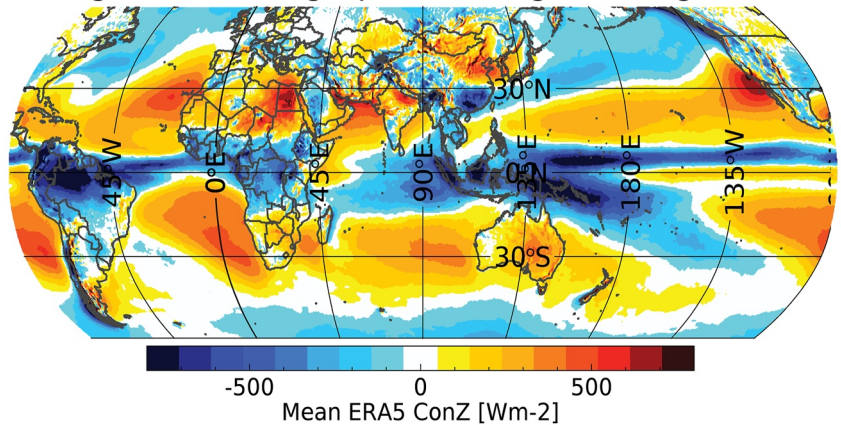


**Figure 4.** Geopotential height energy divergence offsets heating energy changes. (a) 1981–2021 correlations between ERA5 MAM atmospheric heating (diabatic heating + heat convergence) and geopotential height energy divergence. (b) Long term (1981–2021) mean ERA5 atmospheric heating (c) Same for geopotential height convergence.

4.2.1. Atmospheric Heating and the Walker Circulation

As discussed in the methods section atmospheric heating is offset by the divergence of geopotential height energy. During MAM local correlations between these fields are very high (Figure 4a), and these relationships are similar in other seasons and in the MERRA2 reanalysis. Long term mean atmospheric heating (Figure 4b)

and geopotential divergence fields (Figure 4c) help delineate the low- and high-pressure cells that comprise the global Walker Circulation.

Climatologically, the atmospheric heating that drives the Walker Circulation can be visualized by examining maps of vertically integrated diabatic heating (Figure 5a) and atmospheric heat convergence (Figure 5b). These are the two terms on the right-hand side of Equation 3. In the tropics, diabatic heating in the lower and middle troposphere destabilizes the atmosphere and produces lower surface pressures, which drives atmospheric heat convergence (Figure 5b). We refer to the combination of diabatic heating and heat convergence as atmospheric heating. Because temperatures and water vapor are both larger in the lower troposphere, vertically integrated heat and moisture transports are very similar. Areas with strong moisture convergence will have heavy precipitation, strong heat convergence, and large amounts of water vapor that will trap longwave radiation. In the Indo-Pacific, this region of convergence is often referred to as the “Warm Pool”. Figures 5a and 5b also show long-term average moisture transports. The Pacific Trade winds feed very large transports of heat and moisture into the Warm Pool, linking the Walker Circulation to Pacific SSTs.

In MAM, the Indian Ocean branch of the Walker Circulation can be characterized by strong atmospheric heating ( $>450 \text{ Wm}^{-2}$ ) over the eastern equatorial Indian Ocean due to strong diabatic heating and heat convergence (Figures 5a and 5b) and moderate-to-strong heat divergence ( $<-250 \text{ Wm}^{-2}$ ) over the southern, northern, and western equatorial Indian Ocean (Figure 5b). Across the southern Indian Ocean ( $\sim 60\text{--}110^\circ\text{E}$ ), a meridional gradient between extra-tropical cooling (blue shades near  $30^\circ\text{S}$  in Figure 5b) and tropical heating (red shades near  $5^\circ\text{S}$  in Figure 5b), helps produce a strong sea level pressure gradient associated with low-level easterly moisture transports. These turn southeasterly to cross the equator and bring moisture into EA (arrows in yellow boxes Figures 5a and 5b). Over the western and central equatorial Indian Ocean, the zonal east-west heating gradient (Figure 5b) supports an east-west response in vertical velocities (Figure 5c) that helps suppress rainfall over EA. Longitude-by-height transects of climatological equatorial ( $5^\circ\text{S}\text{--}5^\circ\text{N}$ ) ERA5 vertical velocities and zonal velocities reveal, on average, descending air tendencies between  $40$  and  $55^\circ\text{E}$  that heat and stabilize the atmosphere over the eastern Horn of Africa (Figure 5c). Thus, in the long-term mean climate over the Indian Ocean and EA, there are offsetting contributions from atmospheric heating over the Indian Ocean Warm Pool. These heating gradients guide the onshore moisture transports, but also produce subsidence over EA.

#### 4.2.2. Atmospheric Heating and SST During WVG Events

We next explore WVG SSTs and atmospheric heating anomalies. The composite mean WVG SST (Figure 5d) and atmospheric heating anomalies (Figure 5e) exhibit substantial warming in the Western V region and cool anomalies in the east Pacific. WVG events are also associated with large statistically significant changes in atmospheric heating in the Indo-Pacific Warm Pool ( $100\text{--}150^\circ\text{E}$ ,  $15^\circ\text{S}\text{--}15^\circ\text{N}$ ) and the central Pacific ( $150^\circ\text{E}\text{--}170^\circ\text{W}$ ,  $8^\circ\text{S}\text{--}6^\circ\text{N}$ ). There are also notable changes in the northern ( $60\text{--}100^\circ\text{E}$ ,  $15^\circ\text{S}\text{--}6^\circ\text{N}$ ) and central Indian Ocean ( $60\text{--}100^\circ\text{E}$ ,  $15^\circ\text{S}\text{--}6^\circ\text{N}$ ) (Figure 5e). Table 4 lists the diabatic heating, heat convergence, and moisture convergence anomalies for these regions during WVG events. It also lists the difference between 1981 and 2022 dry-versus-wet EA MAM seasons. Over the Pacific, these results identify a large westward transition in equatorial heating. Large changes in diabatic heating and heat convergence produce a westward shift in atmospheric heating, with increased subsidence near the equatorial dateline, increased equatorial Pacific moisture and heat transports, and increased Warm Pool atmospheric heating. There are statistically significant increases in atmospheric heating over the northern Indian Ocean and some small atmospheric heating decreases over the central Indian Ocean.

Over the Indian Ocean, WVG SST anomalies show SST cooling in the central Indian Ocean and warming in the southwestern Indian Ocean (Figure 5d). This Indian Ocean SST gradient is associated with moisture transport anomalies that flow across the southern Indian Ocean, cross the equator near, and then turn east, toward the eastern Indian Ocean (Figure 5e and Table 4). These transport anomalies exhibit enhanced anticyclonic flow that deflects moisture southward along the western flank of the Mascarene High, near  $20^\circ\text{S}$  and  $55^\circ\text{E}$ . This is consistent with findings of Wainwright et al. (2019), indicating that the late onset of MAM rainfall is linked to warmer SSTs over the southwestern Indian Ocean and delays in the northward movement of the tropical rainfall belt. Wainwright et al. (2019) linked warm Arabian Sea SST to earlier cessation, and Figure 5d also indicates such warming.

Atmospheric heating composites for WVG events show above-average heating in the Warm Pool and northern Indian Ocean, west of southern India. This increased heating, combined with less heating over the central

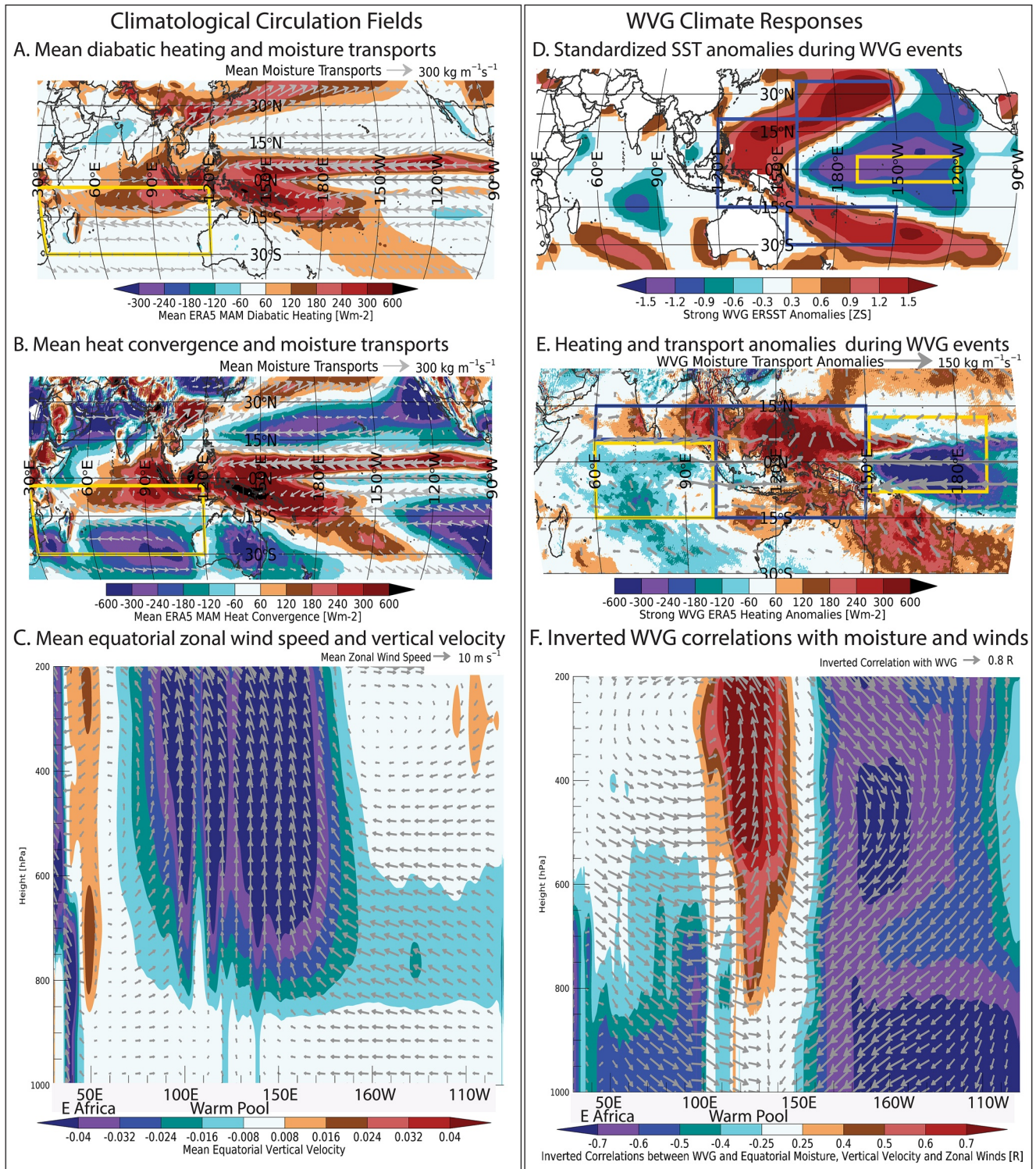


Figure 5.

Indian Ocean, appears associated with anomalous westerly moisture transports across the equatorial Indian Ocean, away from EA. This can be seen as an eastward shift of the climatological transport fields, which typically flow into EA (Figure 5b). These exchanges of heat and moisture modulate the Walker Circulation, increasing heating and moisture convergence over the Warm Pool and northern Indian Ocean, and decreasing

**Table 4**  
Dry-Versus-Wet EA MAM Seasons and WVG Season Anomalies for Selected Forcing Regions

	Warm pool	Eq central Pacific	Northern Indian	Central Indian
Dry-versus-Wet Seasons				
Heat Convergence [ $\text{Wm}^{-2}$ ]	+78***	-85*	+51**	-32**
ERA5	+95***	-130**	+42**	-14
MERRA2				
Diabatic Heating [ $\text{Wm}^{-2}$ ]	+44***	-32	+29**	-13**
ERA5	+77***	-55**	+45**	+3
MERRA2				
Geopotential Divergence [ $\text{Wm}^{-2}$ ]	+108***	-112**	+67**	-51**
ERA5	+128***	-178**	+63**	-16
MERRA2				
Moisture Convergence [mm]	+85***	-80	-45**	-49***
MERRA2	+102***	-128**	-51**	-27*
ERA5				
WVG Seasons				
Heat Convergence [ $\text{Wm}^{-2}$ ]	+123***	-178***	+81***	-49***
ERA5	+133***	-206***	+74**	-36**
MERRA2				
Diabatic Heating [ $\text{Wm}^{-2}$ ]	+66***	-81***	+48***	-19**
ERA5	+95***	-114***	+86***	-40
MERRA2				
Geopotential Divergence [ $\text{Wm}^{-2}$ ]	+169***	-250***	+110***	-76***
ERA5	+172***	-287***	+160***	-91**
MERRA2				
Moisture Convergence [mm]	+121***	-206***	+77***	-75***
ERA5	+126***	-243***	+81***	-59
MERRA2				

Note. \*\*\* denote significance at  $p = 0.1, 0.05,$  and  $0.01,$  based on two-tailed  $T$ -tests. Moisture convergence is shown as the seasonal total moisture convergence. Region coordinates are provided in Section 4.2.2 and Figure 5e. Energy terms are in  $\text{Wm}^{-2},$  while moisture convergence is in total mm per MAM season.

these quantities over the central Indian and Pacific Ocean. The dry season SST composites (Figure 2a) showed fairly large ( $-1.2$  to  $-0.6\text{Z}$ ) and significant cooling anomalies over the central Indian Ocean, which suggest that this often materializes as an enhanced equatorial SST gradient between the central Indian Ocean and the Warm Pool.

As discussed in the methods section, areas of increased or decreased atmospheric heating also correspond to areas with decreasing or increasing divergence of geopotential height energy (Figure 4), because heating and geopotential height energy are tightly coupled in a hydrostatic atmosphere (Peixoto & Oort, 1992). In the central Pacific and central Indian Ocean, increased geopotential height energy convergence stabilizes the atmosphere and increases surface pressures. Conversely, in the Warm Pool and northern Indian Ocean, we find increased geopotential height energy divergence and lower surface pressures. This supports strong zonal moisture and heat transport anomalies flowing from over the central Indian and Pacific Ocean regions into the Warm Pool (Figure 5e).

**Figure 5.** Relating WVG events to Walker Circulation intensification. (a) Mean 1981–2021 ERA5 diabatic heating in  $\text{Wm}^{-2}.$  Vectors show ERA5 mean vertically-integrated moisture transports, with a maximum westerly flux rate of  $-357 \text{ kgm}^{-1}\text{s}^{-1}.$  (b) Same but for mean vertically integrated atmospheric heat convergence. (c) Long term mean ERA5 equatorial [ $5^{\circ}\text{S}$ – $5^{\circ}\text{N}$ ] longitude-by-height vertical and zonal velocities ( $\text{Pas}^{-1}$  and  $\text{ms}^{-1}.$ ) Vertical velocities scaled by 200. The largest negative (upward) vertical velocity is  $-0.07 \text{ Pas}^{-1}.$  The largest easterly zonal velocity is  $8.6 \text{ ms}^{-1}.$  (d) Composites of standardized MAM SSTs during WVG events (circles in Figure 1B). Screened for significance at  $p < 0.1$  using a two-tailed  $t$ -test. (e) Similar composites but for ERA5 atmospheric heating (diabatic heating + atmospheric heat convergence) in  $\text{Wm}^{-2}.$  Screened for significance at  $p < 0.1.$  Also shown are ERA moisture transport anomalies, with a maximum westerly flux rate of  $-174 \text{ kgm}^{-1}\text{s}^{-1}.$  Also shown are areas of interest: Indo-Pacific [ $100$ – $150^{\circ}\text{E}, 15^{\circ}\text{S}$ – $15^{\circ}\text{N}$ ], central Pacific [ $150$ – $170^{\circ}\text{E}, 8^{\circ}\text{S}$ – $12^{\circ}\text{N}$ ], northern Indian Ocean [ $60$ – $100^{\circ}\text{E}, 5^{\circ}\text{N}$ – $15^{\circ}\text{N}$ ], and central Indian Ocean [ $60$ – $100^{\circ}\text{E}, 15^{\circ}\text{S}$ – $5^{\circ}\text{N}$ ]. (f) Shading indicates 1981–2022 correlations between equatorial ERA5 moisture (specific humidity) and inverted observed WVG values. Arrows indicate inverted correlations with vertical and zonal velocities. Since negative vertical velocities (in  $\text{Pas}^{-1}.$ ) indicate upward motions (panel C), the vertical velocity correlations have been inverted, to indicate that stronger WVG values are associated with increased ascent over the Warm Pool. The largest zonal correlations are  $\pm 0.9.$  The largest vertical velocity correlations are  $\pm 0.8.$

**Table 5**  
WVG Season Anomalies for Eastern East African MERRA2 and ERA5 Total Precipitable Water and 600 hPa Vertical Velocities

	Total precipitable Water [kgm <sup>2</sup> s <sup>-1</sup> ]	Total precipitable Water [Z-score]	600 hPa vertical velocity [Pa s <sup>-1</sup> ]	600 hPa vertical velocity [Z score]
ERA5	-2.4***	-1.1Z***	+0.004**	+0.7Z
MERRA2	-2.2***	-1.0Z***	+0.003*	+0.5Z

Note. \*\*\*\* denote significance at  $p < 0.1, 0.05, \text{ and } 0.01$ , based on two-tailed  $t$ -tests. Anomalies expressed as both arithmetic and standardized anomalies. Eastern East Africa region corresponds to an area of Kenya, Ethiopia and Somalia between 38–52°E and 5°S–8°N.

Stronger Pacific SST gradients are associated with increased ascent over the Warm Pool. Correlations between WVG values and equatorial 1981–2022 WVG/ERA5 vertical velocities, zonal velocities, and specific humidity (Figure 5f) reveal a Walker Circulation enhancement, consisting of a Warm Pool versus central Pacific dipole, and a weaker but still significant response over the Indian Ocean. The latter appears associated with subsidence in the middle and lower troposphere, westerly wind anomalies, and reduced atmospheric water vapor in the lower half of the troposphere between 40°E and 100°E. As discussed in Section 4.2.1, climatological conditions relate equatorial Indian Ocean Warm Pool atmospheric heating to offsetting factors: moisture transports across the southern Indian Ocean (Fig. 5AB) and subsidence between 40 and 55°E. WVG events increase atmospheric heating over the northern Indian Ocean and decrease atmospheric heating over the central Indian Ocean (Figure 5e and 5Table 4), while also increasing the zonally overturning Walker Circulation (Figure 5f). Over East Africa, this reduces atmospheric moisture and vertical motions in the mid-troposphere (Table 5).

### 4.2.3. Moisture Transports Over East Africa During Post-1997 MAM WVG Events

Figure 6 provides more spatially detailed analysis of the East Africa/WVG teleconnection. Figure 6a shows the frequency of below-normal MAM CHIRPS rainfall during the 12 WVG seasons. The EA region corresponds fairly well with areas receiving onshore moisture transports during MAM (Figure 6b). Driven by strong pressure gradients in the southern Indian Ocean (Figure 5b), these transports form the Somali Jet which flows across northern Tanzania, eastern Kenya and southern Somalia. During MAM, in south-eastern Ethiopia, northern Kenya, eastern Kenya and central Kenya, these south-easterly flows are associated with precipitation events (Levin et al., 2009). While WVG rainfall composites do identify some dry tendencies in northern Ethiopia (Figure 6a), this region is dominated by boreal summer rains, which have an inverse relationship with La Niña (Korecha & Barnston, 2007).

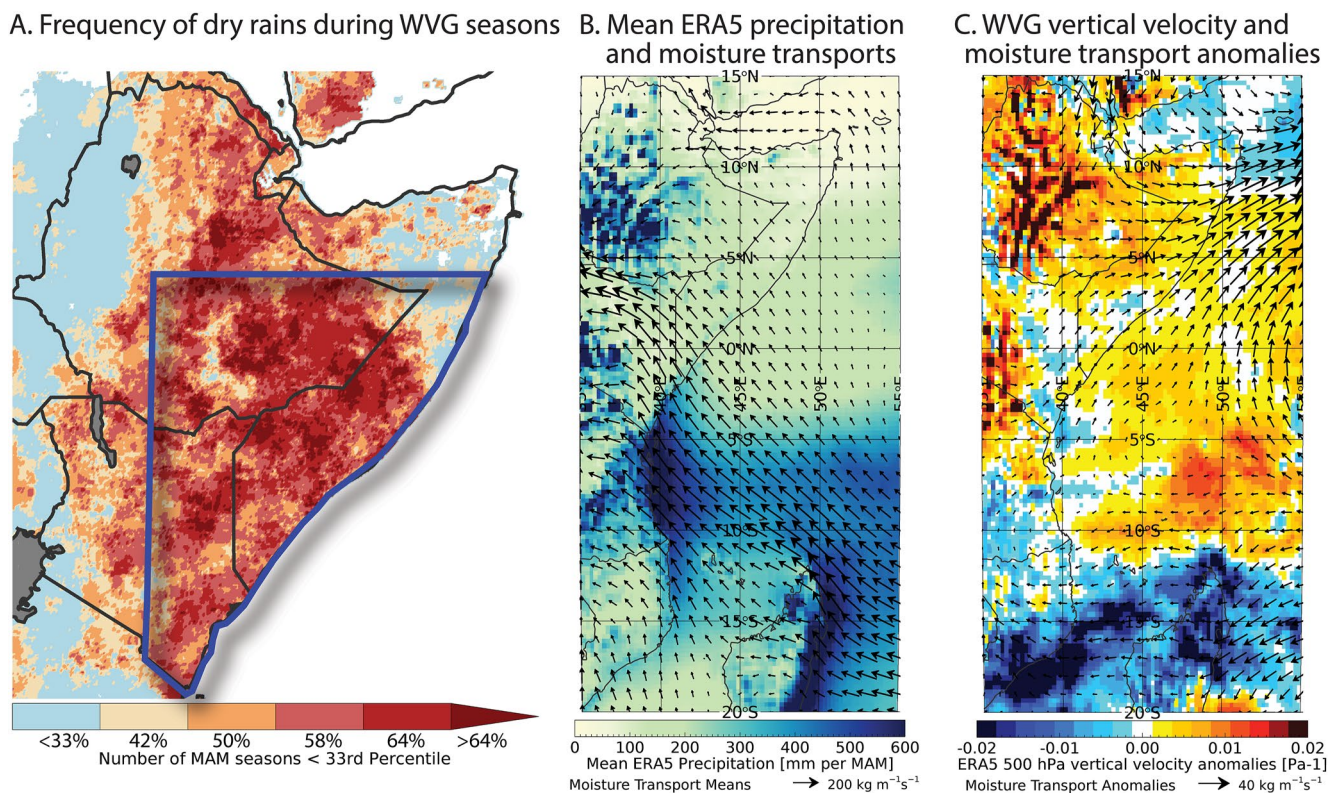


**Figure 6.** Spatially detailed maps describing the WVG teleconnection. (a) The frequency of below-normal MAM CHIRPS seasons during WVG events. (b) 1981–2022 mean ERA5 MAM precipitation and moisture transports. (c) ERA5 500 hPa vertical velocity anomalies and moisture transport anomalies during MAM WVG events.



Boreal summer rains in this region are also primarily supported by moisture from the north and west (Viste & Sorteberg, 2013), though substantial moisture flows originate from the Indian Ocean as well. Thus, the fairly homogeneous negative rainfall response over the EA region (Figure 6a) appears related to substantial and significant reductions in total precipitable water and mid-tropospheric vertical velocities (Table 5). Mid-troposphere (500 hPa) MAM vertical velocity anomalies during WVG seasons (Figure 6c) tend to highlight humid higher elevation areas, and in drought years this subsidence can often be associated with increased air temperatures and impacts in key crop growing areas. In southern Somalia and eastern Kenya, the mid-tropospheric vertical velocity signal is weak, but analysis of zonal equatorial teleconnections (Figure 5f) identifies subsidence and reduced atmospheric water vapor low in the troposphere, below 850 hPa.

Over the eastern Horn, WVG moisture transport anomalies indicate more southwesterly flows (Figure 6c), while across south-eastern Africa (below 15°S), easterly moisture transports increase and upward velocities increase. The latter phenomena appears related to changes in the seasonal cycle leading to shorter long rains growing seasons (Wainwright et al., 2019). In Figures 5c 6c and 5e, we see, respectively, strong subsidence and reductions in atmospheric heating. This stabilization appears associated with the strong southwesterly moisture transport anomalies near 50°E and 5°N (Figure 6c). This pattern resembles climatological JAS conditions (see Figure 8b in Levin et al., 2009), and may be indicative of an earlier cessation, as discussed in Wainwright et al. (2019). As WVG conditions increase the strength of Walker Circulation, subsidence over the western Indian Ocean may support boreal summer-like Indian Ocean moisture transports. This conjecture is supported by WVG increases and reductions atmospheric heating over the northern and central Indian Ocean (Table 4).

#### 4.2.4. Links Between Walker Circulation Enhancement and Frequent EA Droughts

Strong links between an enhanced Walker Circulation and dry outcomes during the EA MAM season are shown in Figures 7a and 7c. These scatterplots identify the very strong covariation between Warm Pool heating and moisture convergence (ERA5  $R = 0.99$ ,  $p < 0.001$ ). This strong correlation is not surprising. Heat and moisture transports are very similar, being driven primarily by low-level winds. Increased moisture convergence increases precipitation and latent heating (Equation 4). More moisture increases the trapping of longwave radiation. What is striking, however, is (a) how variable these terms are, and (b) how well intense heating and moisture convergence discriminates dry EA seasons from wet and normal seasons, as indicated by the circle colors.

The first point matters. If year-to-year variations in Warm Pool heating were small, they would not be likely drivers of EA droughts. But what we see in the ERA5 reanalysis is a very large range, with heating and moisture convergence ranging from  $\sim 150$  to  $\sim 600$   $\text{Wm}^{-2}$  and  $\sim 50$  to  $\sim 350$  mm per MAM season. Hence, these data exhibit a  $\sim$ six-fold change between the weakest and strongest seasons. During the more intense seasons, when ERA5 heating exceeds  $\sim 450$   $\text{Wm}^{-2}$ , as indicated by the vertical black line in Figures 7a and 7c, we see frequent dry EA outcomes and few wet or normal seasons. Furthermore, the circles with green crosses reveal that many of these strong heating/convergence years are strong MAM WVG events that followed OND La Niñas. Thus, OND La Niñas are very robust indicators of strong MAM Warm Pool heating and moisture convergence up to 6 months in the future. Interestingly, the 2018 WVG was associated with only moderate heating and convergence values, as noted in Figure 7a. This season also experienced very heavy rains, likely due to the influence of sub-seasonal MJO and cyclone influences (Kilavi et al., 2018). It should be noted, also, that moderate and low heating/convergence outcomes have few droughts, but there does not appear to be a strong connection to wet season frequencies. These results support the idea that dry seasons are predictable because of links to Pacific SSTs (Figure 2a), while wet seasons are less predictable (Figure 2b), because forcing from Warm Pool is limited.

Scatterplots showing Warm Pool heating and Western V SSTs (Figure 7b) also support links between Western V warming, Walker Circulation enhancements and frequent EA droughts. Warm Pool heating is strongly linked to warmer Western V SSTs. The 1981–2022 correlations between Western V SSTs and ERA5 atmospheric heating are 0.74 (df. 40,  $p = 0.001$ ). Very warm Western V SSTs are clearly associated with increased Warm Pool atmospheric heating, and when Western V SSTs exceed  $+0.8Z$ , we find frequent dry EA rainy seasons (8 out of 12 seasons). We have already discussed the strong link between Western V SSTs and human-induced warming (Figures 3a and 3b). The MAM 2018 season, also identified in Figure 7b, exemplifies that strong negative WVG values can co-exist with modest Warm Pool heating. Not every WVG season exhibits strong Walker Circulation intensification.

There is a robust relationship between ERA5 Warm Pool Atmospheric heating and the frequency of MAM dry seasons, as exemplified by the logistic regression results displayed in Figure 7c. The coefficients of this model are significant at  $p < 0.01$ . The model presents a fairly linear relationship between heating and the chance of drought.

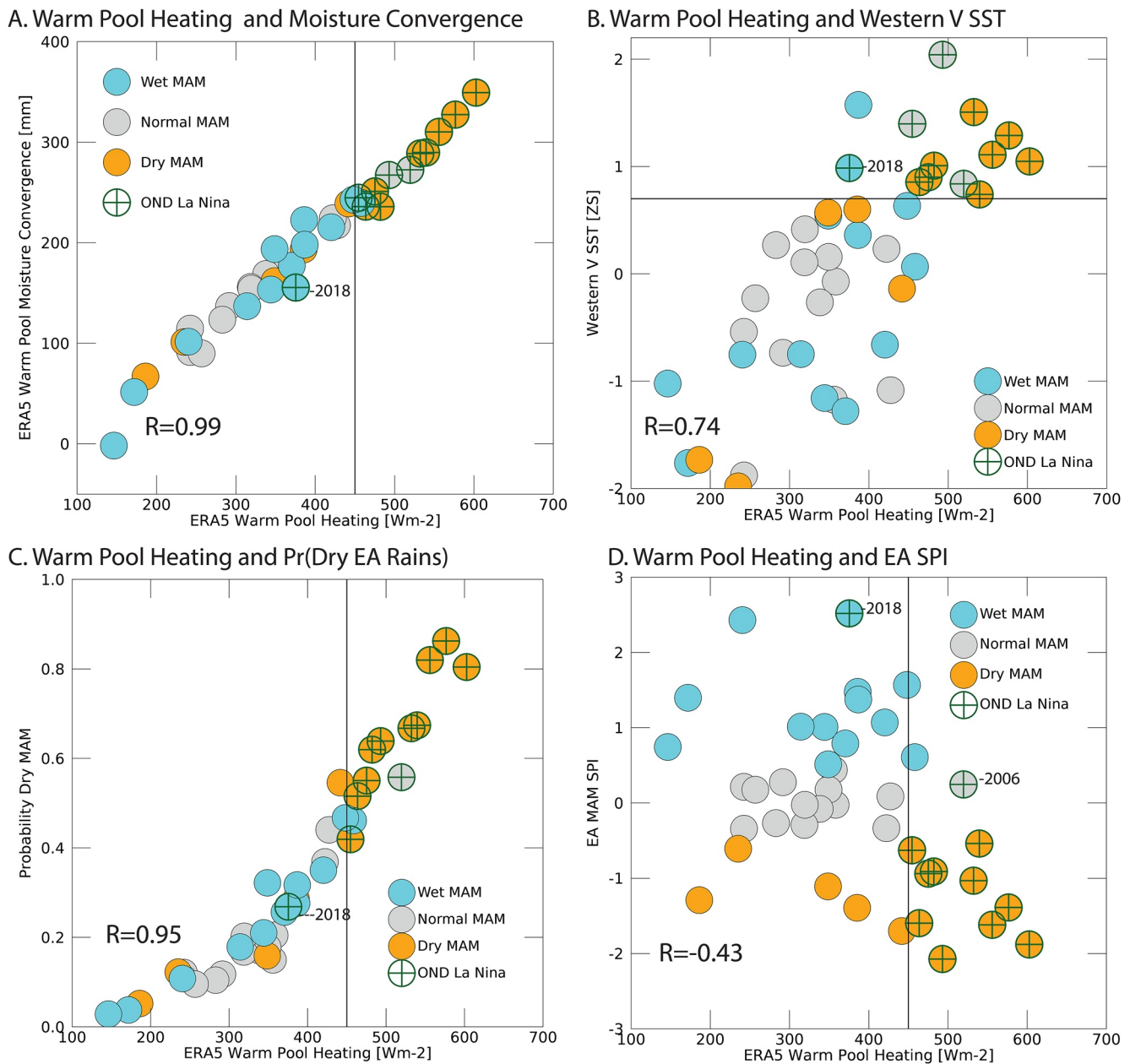
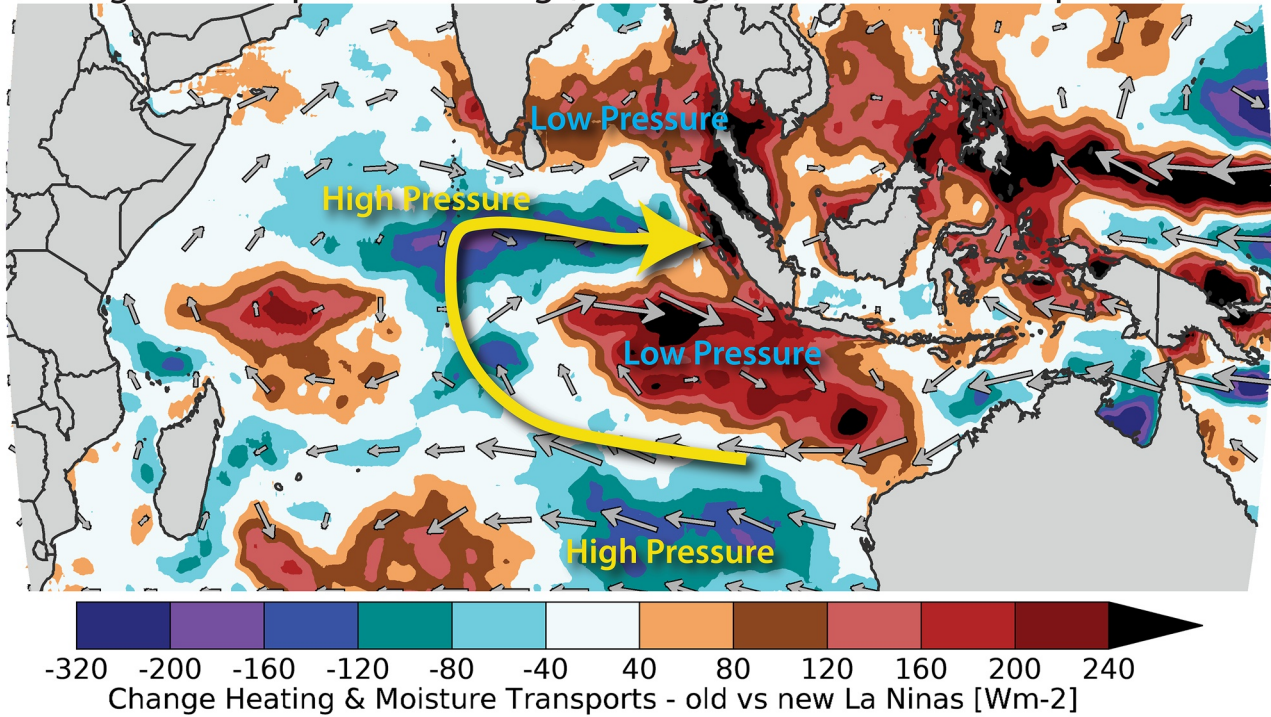


**Figure 7.** Increased Warm Pool atmospheric heating can help explain the predictability of dry EA MAM rainy seasons. Circle color denotes East African MAM rainfall terciles. Green crosses identify preceding OND La Niña seasons. (a) A scatterplot of ERA5 MAM Warm Pool heating ( $x$ -axis) and Warm Pool moisture convergence ( $y$ -axis) (b) A scatterplot of ERA5 Warm Pool heating ( $x$ -axis) and standardized MAM Western V SSTs ( $y$ -axis). Circle colors in (a) and (b) identify EA wet and dry MAM rainy seasons. (c) ERA5 warm pool heating values ( $x$ -axis) along with logistic regression estimates of the probability of below-normal MAM seasons ( $y$ -axis). (d) ERA5 Warm Pool heating and contemporaneous EA MAM SPI values.

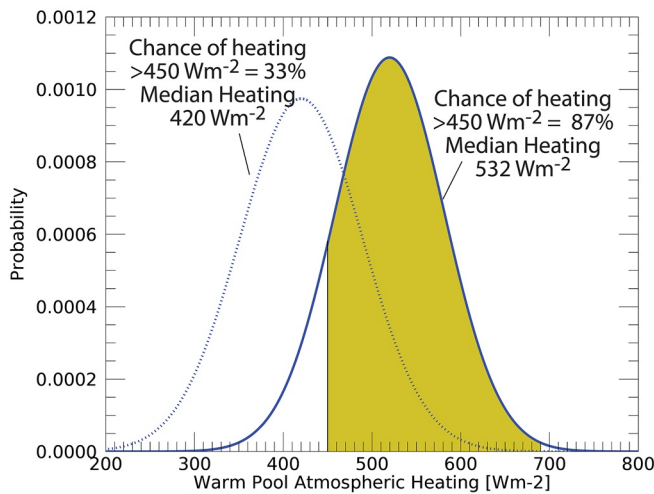
If heating increases by  $100 \text{ Wm}^{-2}$ , the chance of a dry event increases by  $\sim 20\%$ . This regression performs well in terms of dry season identification. When heating exceeds  $\sim 450 \text{ Wm}^{-2}$ , the model indicates that a dry season is likely, that is, the probability exceeds 50%. This results in 10 hits, 26 correct negatives, five misses, and one false alarm. Some dry seasons were not associated with particularly strong Warm Pool heating (1983, 1992, 2004, 2019, and 2021). The 2006 strong Walker Circulation seasons was not dry. But the overall accuracy of the estimation is strong, providing a hit or correct negative 86% of the time.

Further examinations of scatterplots showing ERA5 and MERRA2 Warm Pool atmospheric heating and EA total precipitable water (not shown) reveal interesting behavior. In ERA5, for example, when heating is below

A. Change in atmospheric heating (shading) and moisture transports (arrows)



B. PDFs of Warm Pool Atmospheric Heating



C. PDFs of East African MAM SPI

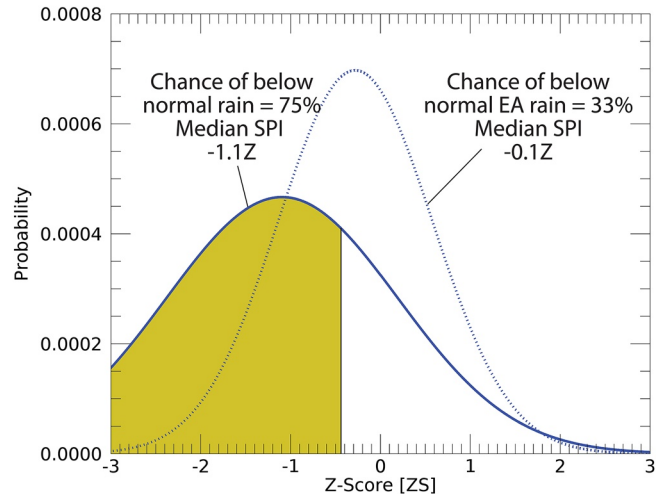


**Figure 8.** Change in atmospheric heating following recent La Niñas can help explain the increased frequency of dry EA rainy seasons. Circle color denotes East African MAM rainfall terciles. Green crosses identify preceding OND La Niña seasons. (a) The difference between 1999–2022 and 1950–1997 ERA5 atmospheric heating and moisture transports in MAM seasons following OND La Niña events. (b) PDFs of MAM West Pacific heating following pre- and post-1998 OND La Niña events. (c) PDFs of EA SPI values for MAM seasons following pre- and post-1998 OND La Niña events. These are based on the SPI values plotted in Figure 1B, subset by La Niña years identified with green circles in Figure 2B.

$\sim 450 \text{ Wm}^{-2}$ , EA MAM precipitable water levels range from 39 to 45  $\text{kg m}^{-2}$ . When heating exceeds this value, moisture levels are lower and range from 36 to 39  $\text{kg m}^{-2}$ . Similarly, over EA, mean mid-tropospheric vertical velocities descend, on average, at twice the velocity when heating exceeds  $450 \text{ Wm}^{-2}$  ( $0.012$  vs.  $0.006 \text{ Pas}^{-1}$ ).

The direct relationship between EA MAM SPI values and Warm Pool heating is relatively weak (Figure 7d), with a 1981–2022 correlation of  $-0.43$  (Figure 7d). This correlation decreases slightly when there has been an OND La Niña to  $-0.63$ , but the intensity of MAM dry seasons is not well estimated. On the other hand, when heating increases beyond  $450 \text{ Wm}^{-2}$ , the mean EA SPI is  $-1Z$  and 9 out of 11 seasons were dry. Conversely, when

heating drops below  $450 \text{ Wm}^{-2}$ , 84% of seasons are **not** dry. Hence Walker Circulation intensity can help bracket seasonal outcomes. As discussed in a recent Earth's Future commentary, more advantage might be taken of anticipated "clemency" (Funk et al., 2023). Implicit in Figure 7 is that when the Walker Circulation is **not** expected to be stronger than normal, the chance of a dry season drops dramatically. This could indicate opportunities for farmers and pastoralists.

Our results also identify opportunities for prediction. As highlighted by the repeated use of green crosses, OND La Niñas are associated with predictable negative MAM WVG values (Figure 2c), strong Warm Pool atmospheric heating, moisture convergence and very warm Western V SSTs (Figure 7). Over eastern East Africa, ERA5 and MERRA2 indicate highly significant and large ( $\sim -1$  sigma) decreases in total precipitable water during WVG MAM seasons; in the mid-troposphere subsidence also increases significantly (Table 5). Often arising in conjunction or after an OND La Niña event, these teleconnections set the stage for sequential dry seasons. Thus, La Niña-related MAM droughts can be anticipated because of reliable and predictable WVG conditions (Figures 2d and 5d) and Walker Circulation enhancements (Figures 5e and 7).

This section has focused on the 1981–2022 satellite-observation period, for which we have good rainfall observations, reanalyses and SST data. Over this period, we can say with great certainty that most MAM EA dry seasons were associated with more heating and moisture convergence in the Warm Pool and northern Indian Ocean, following La Niñas, when there have been predictable very warm Western V and WVG SST conditions. We next shift to a 1950–2022 time period, to explore some of the predominant features that differentiate responses to pre and post-1997 OND La Niña events.

### 4.3. Contrasting MAM Circulations Following 1998–2022 and 1950–1997 OND La Niñas

An important, but analytically challenging, aspect of the EA Paradox is a potential shift in links to La Niña. There is general agreement on a shift in Pacific SST following the 1997/1998 El Niño (L'Heureux et al., 2013; Lyon et al., 2013; Yang et al., 2014). Following this event, Western V SSTs increased (Funk et al., 2019) and the Western V Gradient decreased substantially (Figure 2c). Since the early 2010s, it has been hypothesized that the interaction of La Niña events and a low-frequency warming (Williams & Funk, 2011) may enhance the link between La Niña and dry EA MAM seasons, and recent work on this important topic (Park et al., 2020) shows clearly the increasing correlation between boreal winter ENSO SSTs and EA rains in the following MAM season. Park et al. (2020) describe how a westward intensification of the Walker Circulation enhances links to Pacific SST variations, with 2000–2016 zonal equatorial vertical velocities, 200 hPa velocity potential and winds exhibiting ENSO teleconnections between  $50^\circ\text{E}$  and  $180^\circ\text{E}$ .

The recent availability of 1950–2022 ERA5 reanalysis gives us an exciting opportunity to map the change in atmospheric heating and moisture convergence during the MAM seasons following the 12 post-1997 OND La Niñas versus the 12 1950–1997 La Niñas. The post-1997 MAM La Niña seasons are 1999, 2000, 2001, 2006, 2008, 2009, 2011, 2012, 2017, 2018, 2021, 2022. The pre-1997 seasons are 1955, 1956, 1965, 1971, 1972, 1974, 1975, 1976, 1984, 1985, 1989, and 1996. La Niña seasons are based on OND ONI values  $< -0.5^\circ\text{C}$ .

These results contrast MAM atmospheric heating and moisture transport conditions following "new" versus "old" La Niñas (Figure 8a). Interestingly, over the Indian Ocean, we see more heating and lower sea level pressures over the eastern equatorial Indian Ocean Warm Pool, and cooling and higher pressures over the central Indian Ocean (Figure 8a). These IOD-like changes appear consistent with an intensification of the Indian Ocean branch of the Walker Circulation. Increased Warm Pool atmospheric heating appears associated with higher pressures over the central Indian Ocean, and northward moisture transport anomalies that cross the equator near  $75^\circ\text{E}$  and turn towards Indonesia. In a sense, the longitude of the climatological moisture transports over the Indian Ocean (Figures 5a and 6b) has shifted east, increasing northward transports over the central Indian Ocean (yellow arrow in Figure 8a). In the Pacific, stronger westward transports from over the central Pacific feed more heat and moisture into the Indian Ocean Warm Pool.

Given the strong relationship between dry EA seasons and Warm Pool atmospheric heating (Figures 7a and 7c), we can contrast ERA5 MAM Warm Pool heating Probability Distribution Functions (PDF) for pre- and post-1997 La Niña events (Figure 8b). A large  $\sim 110 \text{ Wm}^{-2}$  increase in heating is identified, and this distribution shift increases the probability of exceeding a  $450 \text{ Wm}^{-2}$  threshold from 33% to 88% following and OND La Niña. Recent OND La Niñas anticipate much more energetic MAM Walker Circulations. These results can help explain

why predicted WVG events (Figure 2d) are good indicators of elevated EA MAM drought risk, and why there has been a large shift in EA MAM SPI PDFs following pre-and-post 1997 La Niña events (Figure 8c). Since 1998, when there has been an OND La Niña, there have been strong MAM WVG gradients (Figure 2c), very warm Western V SSTs (Figure 5d), and strong Warm Pool heating and convergence (Figure 7). These results, and the large and significant changes shown in Figure 8a, help explain why, since 1997, 75% of the time EA MAM rains are poor (Figure 8c) when a La Niña arrives during boreal fall.

It is important to note, however, that dry EA MAM seasons are linked to the overall Pacific SST gradient structure, not just the Niño 3.4 region (Figure 2a). For example, during three of the nine seasons with boreal fall La Niña and dry MAM outcomes (2001, 2009, and 2017), Niño 3.4 SST values did not meet the ONI La Niña criteria during MAM, yet these seasons had strong negative WVG values and large Warm Pool heating values [ $>450 \text{ Wm}^{-2}$ ].

#### 4.4. Relating Warm Pool Heating and More Frequent Droughts to Anthropogenic Warming in the Western V

We next explore low frequency (20-year) links between MAM Pacific SSTs, Warm Pool heating, and EA dry season frequencies. The value of diagnostic analyses focused on atmospheric heating and moisture transport/convergence patterns (i.e., Sections 4.2 and 4.3) is that they enable us to quantify the changes in climatic forcing associated with SST gradients.

To set the stage for this analysis, we briefly present an updated analysis (Figure 9) of the 1900–2022 ENSO and WPWM principal components (PC), as in Funk and Hoell (2015). ENSO in this study, as in (Lyon et al., 2013), is represented by the first EOF and PC of tropical Pacific SSTs. This PC tracks closely with SST in the Niño 3.4 region (Figure 9a). The ENSO PC and Niño 3.4 average SST time-series have a 1950–2022 correlation of 0.94. To estimate the WPWM, each grid cell's MAM SST is regressed against the ENSO PC. Then the first EOF of the global residuals is used to define the WPWM, which tracks closely with the Western V. The WPWM PC and Western V average SST time-series have a 1950–2022 correlation of 0.87. An identical calculation of the WPWM, based on large ensembles of climate change models, are very similar to the observed patterns (Funk & Hoell, 2015, 2017). In broad strokes, two transitions appear in these PC time-series. First, the ENSO/Niño 3.4 time-series have a Pacific Decadal Oscillation-related (Mantua & Hare, 2002) increase in the late 1970s, but thereafter show little increase (Seager et al., 2022). Then, the WPWM/Western V trends upward, with post-1998 values being especially warm. It is worth noting that the MAM 2022 WPWM and Western V values appear to be, by a substantial margin, the warmest on record. Western V warming is *not* primarily driven by Pacific Decadal Variability, but by human-induced warming.

We next use linear regression to relate 20-year MAM Western V and Niño 3.4 SST values to 20-year 1950–2022 ERA5 Warm Pool atmospheric heating. The blue bars in Figure 10a show 20-year average ERA5 Warm Pool atmospheric heating. Between the first and last 20-year period we see a substantial increase, from  $\sim 340$  to  $\sim 420 \text{ Wm}^{-2}$ . Interestingly, a regression based on 20-year standardized Western V and Niño 3.4 SST can explain 97% of the atmospheric heating variance. The Western V and Niño 3.4 coefficients are highly significant and roughly similar in magnitude (58 and  $67 \text{ Wm}^{-2}$  per standardized anomaly). These results are shown with a green line in Figure 10a. A regression carried out with just 20-year Western V (red line Figure 10a) explains 76% of the observed variance. *Most of the 20-year variance of the Warm Pool heating can be explained by Western V warming.*

We would interpret these results as follows. First, the WVG formulation, which gives equal weight to the Western V and Niño 3.4 regions, seems fairly justified at 20-year time-scales. 20-year Warm Pool atmospheric heating covaries with both 20-year Niño 3.4 and Western V SSTs, which in turn track closely with the first two modes of global SST variability (Figure 9). Between the 1970s and 1990s a largely natural increase in Niño 3.4 SSTs occurred (Mantua & Hare, 2002) (Figure 3c), and we also see this reflected in the Warm Pool heating regression estimate, which declined by about  $40 \text{ Wm}^{-2}$  during this period. However, since the 1980s, the Western V warmed substantially, and we find this associated with a large  $\sim 80 \text{ Wm}^{-2}$  increase Warm Pool heating.

Is the recent Western V warming largely due to climate change, or natural decadal variability? While some studies, using detrended SSTs, have argued that western Pacific warming is largely natural (Lyon, 2014; Yang et al., 2014), it is possible that the detrending process used in these studies introduces biases into the results, since the rates of external forcing and associated warming increase non-linearly. Assuming climate change is a linear trend, and that residuals from this linear trend are “natural” (as in Lyon, 2014), can miss the rapid human-induced warming present in the 1990s–2020s (Figure 3a). A simpler approach is to compare directly observed 20-year

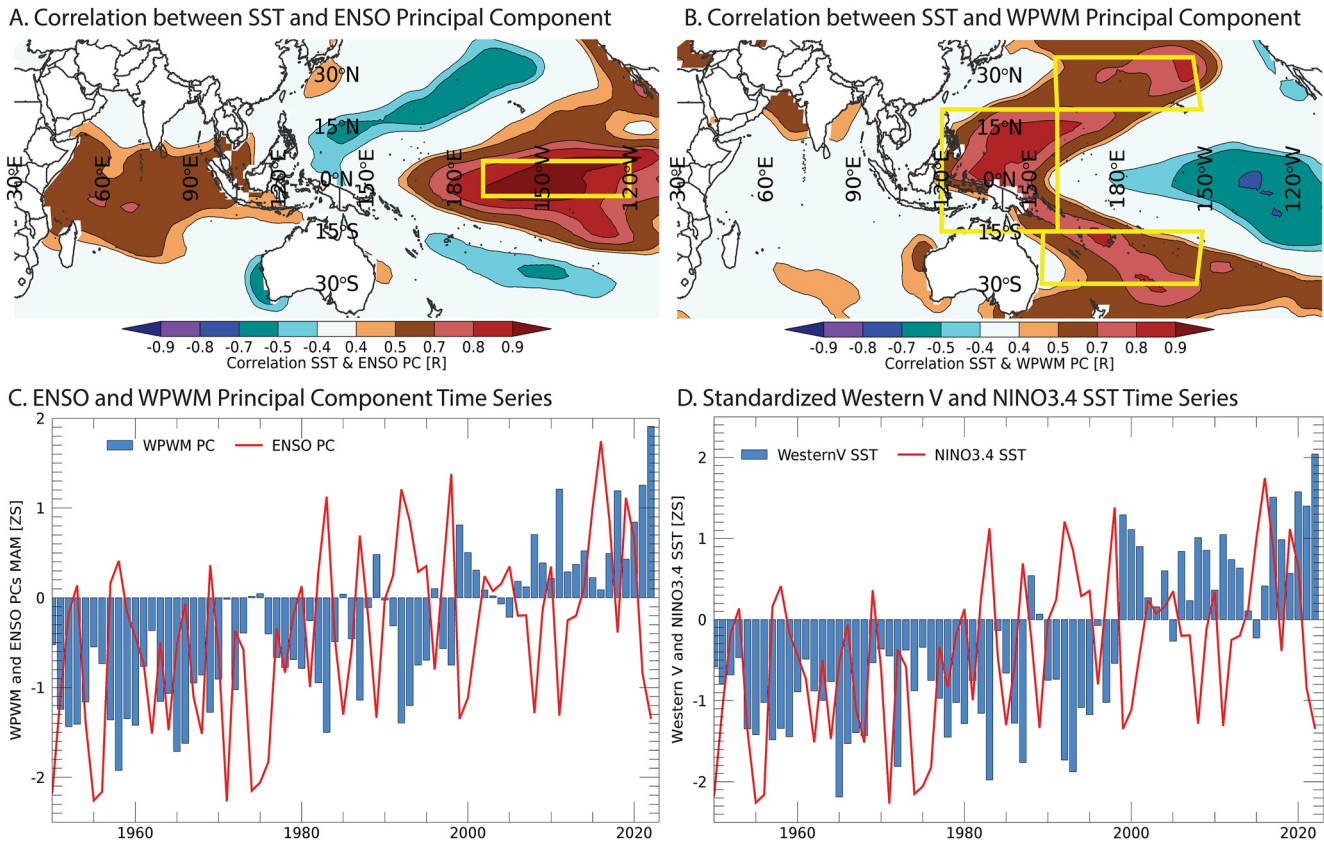


**Figure 9.** Relating MAM Niño 3.4 and Western V SST to ENSO and West Pacific Warming Mode Empirical Orthogonal Functions (EOF). (a) 1981–2022 correlation between the first Principal Component (PC) of tropical Pacific MAM SSTs and observed MAM SSTs. Yellow box denotes the Niño 3.4 region. (b) Same but for the WPWM and Western V region. (c) Time-series of MAM WPWM and ENSO MAM PCs, expressed as standardized anomalies centered on a 1981–2021 baseline. (d) Same for regional SST averaged over the Western V and Niño 3.4.

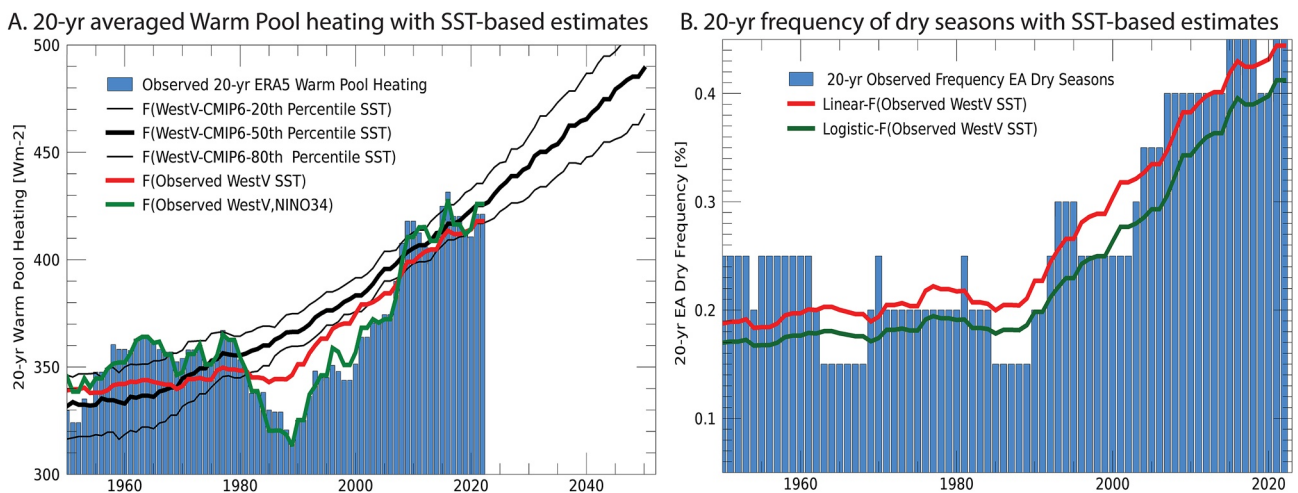


**Figure 10.** Relating Warm Pool heating and more frequent droughts to anthropogenic warming in the Western V. (a) Observed and estimated 20-year ERA5 West Pacific Heating V SST anomalies. The green line shows regression estimates based on observed standardized 20-year Western V and Niño 3.4 SST. The red line shows estimates based only on observed Western V. The thick black line shows 20-year Warm Pool heating based on the median CMIP6 Western V SST estimates. The thin black lines show the spread of CMIP6 Warm Pool Heating estimates. (b) The 20-year observed frequency of EA dry seasons (i.e., circles in Figure 2C), along with Western V-based regression estimates.

Western V SSTs with estimates from the CMIP5 (Funk et al., 2019) or CMIP6 (Figures 3a and 9a). CMIP6 20-year Western V SST tracks extremely well with the observations (median time series,  $R = 0.98$ , 1950–2022). Based on a linear regression model that predicts Warm Pool atmospheric heating with Western V SST 20-year Z scores ( $\text{HEAT}_{\text{WP}} = b_0 + b_1 * \text{Western V SST}$ ), the heavy black line in Figure 10a translates the median CMIP6 Western V SST values into Warm Pool atmospheric heating, in  $\text{Wm}^{-2}$ . In this model the coefficients ( $b_0 = 386 \text{ Wm}^{-2}$ ,  $b_1 = 44 \text{ Wm}^{-2}$ ) are derived from the observed 20-year SST data, and then new heating values are produced by using the ensemble median 20-year CMIP6 SST values for the Western V SST. Figure 10a also shows 20th and 80th percentile CMIP6 estimates produced using this method. Differences between the observed (red line) and externally-forced CMIP6 (heavy black line) 20-year Western V time-series indicate the influence of natural Pacific Decadal Variability. These fluctuations are limited to a small cooling in the 1980s and warming in the late-2000s. The dominant change in observed 20-year running average Western V (red line) - the increasing trend - aligns with human-induced warming (black lines). Between 1950 and 2022, CMIP6 Western V SST estimates suggest an overall increase in Warm Pool atmospheric heating from  $\sim 340$  to  $\sim 410 \text{ Wm}^{-2}$ . This shift in mean Warm Pool heating is augmented further following recent La Niña events (Figure 8a), helping to explain the observed increase in dry EA MAM seasons (33%–75%, Figure 8c).

Over the past 75 years, Western V SSTs have warmed by approximately +2Z standardized anomalies, and the regression results indicate that this warming shifts the mean heating distribution by more than  $+70 \text{ Wm}^{-2}$ . Projections through 2050 suggest a similar increase over the next 30 years, from  $\sim 420$  to  $\sim 490 \text{ Wm}^{-2}$  (Figure 10a). Such heating influences will likely further impact moisture transports and atmospheric stability over EA and the Indian Ocean. These influences will be particularly dangerous during or following La Niñas, setting the stage for more frequent sequential OND/MAM droughts.

In contrast to Western V SSTs, there is a large and growing discrepancy between observed east Pacific SSTs and CMIP6 projections, with “*observations-based SST trends ... at the far edge or beyond the range of modeled internal variability*” (Seager et al., 2022). There has been a notable lack of warming in the Niño 3.4 region, and this is in marked contrast to 20-year anomalies from a 25-model 152-member ensemble of CMIP6 simulations (Figure 3d). The observed 2003–2022 value ( $-0.09 \text{ Z}$ ) is extremely unlikely given the distribution from the CMIP6 simulations (Figures 3c and 3d). More detailed analyses (Wills et al., 2022) identify “*a triangular region in the eastern tropical and subtropical Pacific*” as the ocean region where CMIP6 model simulations differ most from observations, with the differences being very unlikely ( $<5\%$  probability) due to internal variability. While a detailed exploration is beyond the scope of this study, systematic Pacific SST biases are one likely cause of this discrepancy, and when bias-corrected ocean and atmosphere models are used to explore this issue, they recreate the observed increase in equatorial Pacific zonal SST gradients (Seager et al., 2019). Hence, it appears to be problematic to assume that the climate change models are “correct” and that the observed lack of warming is driven by naturally-occurring Pacific Decadal Variability.

Finally, we find that Western V SST increases can explain most of the variance in the frequency of dry seasons at 20-year time scales, that is, the number of times in each 20-year period in which EA MAM SPI was less than  $-0.44 \text{ Z}$  (Figure 10b). A linear regression model ( $\text{PROB}_{\text{dry}} = b_0 + b_1 * \text{Western V SST}$ ;  $b_0 = 0.3$ ,  $b_1 = 0.13$ ) using observed 20-year running averages of Western V SSTs as a predictor and 20-year observed frequencies of dry EA MAM seasons as a predictand recreates a large portion of the variance ( $R^2 = 0.74$ ). The red line in Figure 10b shows these probability estimates, which range from  $\sim 0.20$  in the 1950s through 1980s to values twice as high,  $\sim 0.4$ , after the 2000s. Similar results are found using a logistic regression model. These results suggest that the Western V warming has been a primary driver of increased dry season frequencies in the eastern Horn of Africa. Since Western V warming has been dominated by human-induced external forcing, climate change has been a strong driver of increased dry season frequencies in East Africa. A similar conclusion is represented in Figures 7c and 10a. A human-induced  $80 \text{ Wm}^{-2}$  increase Warm Pool atmospheric heating would be associated with  $\sim 15\%$  increase in the probability of a dry MAM season. This increase combines with natural La Niña-related Walker Circulation enhancements, explaining the robust drought tendency during or following recent La Niñas (Figures 8b and 8c).

## 5. Conclusion: A Walker Circulation Intensification can Explain the Enhanced Predictability of the EA MAM Rains

Here, we have addressed a quite specific question: does intensification of the Walker Circulations help explain the fact that so many recent OND La Niñas are followed by below-normal MAM EA rainy seasons? Furthermore,

how does this link relate to climate change and the large observed decline in EA MAM rains (Figure 1b)? We have addressed these questions in a two-step attribution process. The first step links observed EA droughts to increasingly negative Western V Gradient conditions (i.e., Western V SSTs are warming faster than Niño3.4 SSTs) that are also predictable (Figure 2). These strong Pacific WVG SST gradients, we argue, are being produced through an interaction of naturally-occurring La Niña events and human-induced warming in the Western V region (Figures 2c, 3a, 3a, and 3b). The second step then links WVG events to changes in the Walker Circulation and conditions over EA (Figures 5–7, Tables 4 and 5).

Scatterplots of Warm Pool atmospheric heating and moisture convergence (Figure 7a) very strongly support the link between Walker Circulation enhancements and dry EA outcomes. When ERA5 heating exceeded  $450 \text{ Wm}^{-2}$  there were 9 dry seasons, 2 normal seasons and 2 wet seasons. Strong Warm Pool heating in MERRA2 reanalyses similarly discriminate dry outcomes.

As previously hypothesized, Walker Circulation enhancements are a robust indicator of dry EA outcomes. Twelve post-1997 La Niñas were precursors to MAM SST anomalies (Figure 5d) that strongly resemble dry season SST composites (Figure 2a). The associated circulation disruptions (Figure 5e, Fig. 8AB, Table 4) appear linked to frequent droughts (Figure 1b). Altogether, these connections offer opportunities for prediction (Figure 2d). The energetic framework provided here helps us explain these opportunities. While we only have ~12 events, we see that Warm Pool heating and moisture convergence increases dramatically during almost all of these seasons (Figures 7a and 7c) and when compared to the MAM seasons following 1950–1997 La Niñas (Figures 8a and 8b).

Thus, without ruling out other influences such as westerly Congo Basin moisture transports and the MJO (Finney et al., 2020), or sub-seasonal changes in the length of the long rains (Wainwright et al., 2019), the results presented here support the idea that one primary cause of recent EA droughts has involved a large westward shift in atmospheric heating between the equatorial central Pacific and Warm Pool regions during WVG seasons. These regions exhibit the largest atmospheric heating anomalies. But, as shown in the early 1980s (Gill, 1980), increased heating in the Warm Pool may increase subsidence and low-level pressures to the west, changing circulation patterns over the Indian Ocean, providing proximate impacts that reduce moisture and vertical ascent over East Africa. Early studies linking EA drying with an increased Indian Ocean branch of the Walker Circulation posited atmospheric heating over the central Indian Ocean (Funk et al., 2008; Verdin et al., 2005); the work presented here suggests heating increases over Indian and Pacific Warm Pool regions, and underscores the amplifying role played by moisture and heat transports and convergence. This helps explain the link with Pacific SSTs (Lyon & DeWitt, 2012; Yang et al., 2014) as well as the tendency for the long rains to start later and end earlier (Wainwright et al., 2019). Such insights could assist in the prediction of onset and cessation dates, which are linked to zonal wind variations over the Indian Ocean (MacLeod, 2018).

Our WVG composites (Figure 5d) also identify Indian Ocean SST warming over the southwest and northern Indian Ocean, and cooling near  $75^\circ\text{E}$ ,  $15^\circ\text{S}$ , which may be consistent with a later start and earlier cessation of the long rains. In the southern Indian Ocean, during WVG events (Figure 5d), warmer southwestern SSTs could delay the typical northward progression of the rains between February and March. In the central and northern Indian Ocean, during WVG events (Figures 5d and 5e, Table 4), warmer SSTs (Figure 5d) and increased atmospheric heating (Figure 5e) over the northern Indian Ocean, combined with cooler SSTs and less heating over the central Indian Ocean, might also help trigger an early transition to the boreal summer Indian Monsoon circulation, which could reduce rainfall in May. The contrasting heating responses over the northern and central Indian Ocean (Figure 5e) help drive moisture and heat into the atmosphere over the Warm Pool, and away from EA. A Walker Circulation intensification over the northern Indian Ocean may lead to an earlier transition to a boreal summer monsoon pattern, similar to the June–August circulation. Hence, the increased frequency of strong Pacific SST gradients, especially following recent La Niñas, appears related to the shorter EA rainy season as described by Wainwright et al. (2019). Climate change assessments, based on regional climate model results (Gudoshava et al., 2020), have suggested that the long rains will start and end earlier. This earlier start projection, which appears at odds with the observations, may be related to a tendency for the global climate change models to predict an El Niño-like tendency in Pacific SSTs (Figures 3c and 3d), and the well-established north-south rainfall dipole associated with ENSO, with southern (eastern) Africa being drier (wetter) during El Niños.

In our La Niña atmospheric heating analysis (Figure 8a), we find enhanced atmospheric heating primarily in the south-eastern Indian Ocean, where recent La Niñas appear associated with  $>160 \text{ Wm}^{-2}$  more heating than pre-1998 events. In the absence of strong Walker Circulation forcing, sub-seasonal influences such as the MJO,



and more local weather influences such as westerly Congo basin moisture transports likely play an important role (Finney et al., 2020). The MJO, of course, modulates the Walker Circulation and East African rains as well, and certainly influences heating and moisture transports. Recent research has linked a two-fold expansion of the Warm Pool to a modulation of the MJO life cycle (Roxy et al., 2019), with Maritime Continent residence times increasing by 5–6 days and Indian Ocean residence times decreasing by 3–4 days. Analyses of global satellite-gauge precipitation trends (Adler et al., 2017) have noted marked increases in WVG-like SSTs, Warm Pool total precipitable water and precipitation (cf. their Figure 8), consistent with a strong equatorial Pacific SST gradient (Seager et al., 2019, 2022).

In closing, when one considers the cause of the EA rainfall decline, we would suggest that it is useful to consider two aspects: the increased impacts following recent La Niña events, and the high frequency of recent La Niña events themselves. Here, we have explored why La Niña-related SST conditions have become such a consistent driver of droughts during MAM. Our analysis of atmospheric heating and changes in moisture transports help explain how the combination of anthropogenic Western V warming and La Niña events leads to increases in Warm Pool heating, which in turn modulates important circulation features over the Indian Ocean, increasing subsidence and decreasing EA moisture levels (Table 5). Hence, the interaction of climate change and frequent La Niña events have led to frequent MAM droughts, and many of those dry seasons have followed poor OND outcomes (Funk et al., 2018). This is consistent with recent multi-agency alerts attributing the recent droughts to the combined influence of La Niña and climate change. Without climate change, there would not be a strong link to La Niñas (Figures 8a and 8b). It is worth noting that “strong gradient La Niñas” have been identified in observations (Johnson, 2013), and are expected by climate change model projections later in the 21st century (Cai et al., 2022; Cai et al., 2015a; Cai et al., 2015b).

For EA, our study has emphasized the strong relationship between MAM atmospheric heating, WVG SST and EA SPI, given the set of all post-1997 OND La Niña events. Such conditions pose risks, even if a La Niña event fades. When these events commence, enhanced trade winds transport more oceanic heat energy from the east Pacific and into the Western V region, via the sub-tropical gyre, and there is a great deal of certainty that these transports will persist for many months. As oceanic heat content increases due to climate change, it is not surprising to see that these natural La Niña transport patterns result in large increases in Western V SSTs, and more negative WVG values (Figure 2c), which are very predictable (Figure 2d). Western V SSTs, even in the absence of very cool Niño 3.4 SSTs, still increase low-level flows of heat and moisture into the Warm Pool atmosphere, which increase the risk of dry EA rainy seasons. Even if the frequency of La Niñas were to decrease in the future, La Niñas will develop in an environment that is very warm and warmer than present, and conditions in the Warm Pool and Western V regions will likely amplify the impacts of these La Niñas, setting the stage for sequential dry East Africa outcomes in OND and MAM. It is also possible, however, that observed streak of La Niñas will continue, due to a stronger zonal Pacific gradient. CMIP6-based projections of Warm Pool atmospheric heating, based on Western V warming, suggest a further  $\sim 70 \text{ Wm}^{-2}$  increase by 2050 (Figure 10a). Understanding the emergent links between La Niñas, WVG and the Walker Circulation will help anticipate and manage future drought risks.

## Data Availability Statement

The rainfall observations, reanalyses time series and CMIP6 time series data used to support the major hypotheses in this study are available at dryad via <https://doi.org/10.25349/D9T034> with no restrictions (Funk, 2023).

## Acknowledgments

This research was supported by the United States Agency for International Development (USAID) (Cooperative Agreement 72DFFP19CA00001), National Aeronautics and Space Administration (NASA) GPM mission Grant 80NSSC19K0686, and the Bill and Melinda Gates Foundation contract INV-017546. We would also like express our gratitude to our anonymous reviewers and our editor, Amir AghaKouchak. Their suggestions have resulted in a much-improved manuscript.

## References

- Adler, R. F., Gu, G., Sapiano, M., Wang, J.-J., & Huffman, G. J. (2017). Global precipitation: Means, variations and trends during the satellite era (1979–2014). *Surveys in Geophysics*, 38(4), 679–699. <https://doi.org/10.1007/s10712-017-9416-4>
- Anderson, W., Cook, B. I., Sliniski, K., Schwarzwald, K., McNally, A., & Funk, C. (2023). Multi-year La Niña events and multi-season drought in the Horn of Africa. *Journal of Hydrometeorology*, 24(1), 119–131. <https://doi.org/10.1175/jhm-d-22-0043.1>
- Bjerknes, J. (1969). Atmospheric teleconnections from the equatorial Pacific. *Monthly Weather Review*, 97(3), 163–172. [https://doi.org/10.1175/1520-0493\(1969\)097<0163:atfep>2.3.co;2](https://doi.org/10.1175/1520-0493(1969)097<0163:atfep>2.3.co;2)
- Button, H. (2022). *Famine Early Warning Systems Network forecasts alert USAID to impending food emergencies*. US Agency for International Development.
- Cai, W., Ng, B., Wang, G., Santoso, A., Wu, L., & Yang, K. (2022). Increased ENSO sea surface temperature variability under four IPCC emission scenarios. *Nature Climate Change*, 12(3), 228–231. <https://doi.org/10.1038/s41558-022-01282-z>

- Cai, W., Santoso, A., Wang, G., Yeh, S. W., Cobb, K. M., et al. (2015a). ENSO and greenhouse warming. *Nature Climate Change*, 5(9), 849–859. <https://doi.org/10.1038/nclimate2743>
- Cai, W., Wang, G., Santoso, A., McPhaden, M. J., Wu, L., Jin, F.-F., et al. (2015b). Increased frequency of extreme La Niña events under greenhouse warming. *Nature Climate Change*, 5(2), 132–137. <https://doi.org/10.1038/nclimate2492>
- Checchi, F., & Robinson, W. C. (2013). Mortality among populations of southern and central Somalia affected by severe food insecurity and famine during 2010–2012 (p. 87).
- Dinku, T., Funk, C., Peterson, P., Maidment, R., Tadesse, T., Gadain, H., & Ceccato, P. (2018). Validation of the CHIRPS satellite rainfall estimates over eastern of Africa. *Quarterly Journal of the Royal Meteorological Society*.
- Endris, H. S., Hirons, L., Segele, Z. T., Gudoshava, M., Woolnough, S., & Artan, G. A. (2021). Evaluation of the skill of monthly precipitation forecasts from global prediction systems over the Greater Horn of Africa. *Weather and Forecasting*, 36, 1275–1298. <https://doi.org/10.1175/waf-d-20-0177.1>
- Endris, H. S., Lennard, C., Hewitson, B., Dosio, A., Nikulin, G., & Artan, G. A. (2019). Future changes in rainfall associated with ENSO, IOD and changes in the mean state over Eastern Africa. *Climate Dynamics*, 52(3–4), 2029–2053. <https://doi.org/10.1007/s00382-018-4239-7>
- Endris, H. S., Lennard, C., Hewitson, B., Dosio, A., Nikulin, G., & Panitz, H.-J. (2016). Teleconnection responses in multi-GCM driven CORDEX RCMs over Eastern Africa. *Climate Dynamics*, 46(9–10), 2821–2846. <https://doi.org/10.1007/s00382-015-2734-7>
- Endris, H. S., Omondi, P., Jain, S., Lennard, C., Hewitson, B., Chang'a, L., et al. (2013). Assessment of the performance of CORDEX regional climate models in simulating East African rainfall. *Journal of Climate*, 26(21), 8453–8475. <https://doi.org/10.1175/jcli-d-12-00708.1>
- Eyring, V., Bony, S., Meehl, G. A., Senior, C. A., Stevens, B., Stouffer, R. J., & Taylor, K. E. (2016). Overview of the coupled model Inter-comparison project phase 6 (CMIP6) experimental design and organization. *Geoscientific Model Development*, 9(5), 1937–1958. <https://doi.org/10.5194/gmd-9-1937-2016>
- Finney, D. L., Marsham, J. H., Walker, D. P., Birch, C. E., Woodhams, B. J., Jackson, L. S., & Hardy, S. (2020). The effect of westerlies on East African rainfall and the associated role of tropical cyclones and the Madden–Julian Oscillation. *Quarterly Journal of the Royal Meteorological Society*, 146(727), 647–664. <https://doi.org/10.1002/qj.3698>
- Funk, C. (2023). Dataset - frequent but predictable droughts in East Africa driven by A Walker circulation intensification [Dataset]. CHC Ed. Dryad. <https://doi.org/10.25349/D9T034>
- Funk, C., Dettinger, M. D., Michaelsen, J. C., Verdin, J. P., Brown, M. E., Barlow, M., & Hoell, A. (2008). Warming of the Indian Ocean threatens eastern and southern African food security but could be mitigated by agricultural development. *Proceeding of National Academy of Science USA*, 105(32), 11081–11086. <https://doi.org/10.1073/pnas.0708196105>
- Funk, C., Senay, G., Asfaw, A., Verdin, J., Rowland, J., Korecha, D., et al. (2005). In F. NET (Ed.), *Recent drought tendencies in Ethiopia and equatorial-subtropical eastern Africa. Vulnerability to food insecurity: Factor Identification and characterization report* (Vol. 12). US Agency for International Development.
- Funk, C., Peterson, P., Landsfeld, M., Pedreros, D., Verdin, J., Shukla, S., et al. (2015). The climate hazards infrared precipitation with stations—A new environmental record for monitoring extremes. *Scientific Data*, 2. <https://doi.org/10.1038/sdata.2015.66>
- Funk, C., Harrison, L., Segele, Z., Rosenstock, T., Steward, P., Anderson, C. L., et al. (2023). Tailored forecasts can predict extreme climate informing proactive interventions in East Africa. *Earth's Future*. <https://doi.org/10.1029/2023ef003524>
- Funk, C., & Hoell, A. (2015). The leading mode of observed and CMIP5 ENSO-residual sea surface temperatures and associated changes in Indo-Pacific climate. *Journal of Climate*, 28(11), 4309–4329. <https://doi.org/10.1175/jcli-d-14-00334.1>
- Funk, C., & Hoell, A. (2017). In S. Y. Wang, Y. Jin-Ho, C. Funk, & R. Gillies (Eds.), *Recent climate extremes associated with the West Pacific warming mode. Climate extremes: Patterns and mechanisms*. Wiley Press
- Funk, C., Hoell, A., Shukla, S., Bladé, I., Liebmann, B., Roberts, J. B., & Husak, G. (2014). Predicting East African spring droughts using Pacific and Indian Ocean sea surface temperature indices. *Hydrology and Earth System Sciences Discussions*, 11(12), 3111–3136. <https://doi.org/10.5194/hess-18-4965-2014>
- Funk, C., Nicholson, S., Hoell, A., Korecha, D., Galu, G., Artan, G., et al. (2019). Examining the potential contributions of extreme 'Western V' sea surface temperatures to the 2017 March–June East African Drought. *Bulletin of American Meteorological Society*, 100(1), S55–S60. <https://doi.org/10.1175/bams-d-18-0108.1>
- Funk, C., Shukla, S., Pomposi, C., Galu, G., Korecha, D., Husak, G., et al. (2018). Examining the role of unusually warm Indo-Pacific sea surface temperatures in recent African droughts. *Quarterly Journal of Royal Meteorological Society*, 144(S1), 360–383. <https://doi.org/10.1002/qj.3266>
- Funk, C., Turner, W., McNally, A., Hoell, A., Harrison, L., Galu, G., et al. (2021b). An agro-pastoral phenological water balance framework for monitoring and predicting growing season water deficits and drought stress. *Frontiers in Climate*, 3. <https://doi.org/10.3389/fclim.2021.716568>
- Funk, C., Way-Henthorne, J., & Turner, W. (2021). Phenological water balance applications for trend analyses and risk management. *Frontiers in Climate*, 3. <https://doi.org/10.3389/fclim.2021.716588>
- Gelaro, R., Suárez, M. J., Todling, R., Molod, A., Takacs, L., Randles, C. A., et al. (2017). The Modern-era Retrospective analysis for research and applications, version 2 (MERRA-2). *Journal of Climate*, 30(14), 5419–5454. <https://doi.org/10.1175/jcli-d-16-0758.1>
- Gill, A. E. (1980). Some simple solutions for heat-induced tropical circulation. *Quarterly Journal of Royal Meteorological Society*, 106(449), 447–462. <https://doi.org/10.1002/qj.49710644905>
- Gill, A. E. (1982). *Atmosphere-ocean dynamics* (Vol. 30). Academic Press. 662 pp.
- Gudoshava, M., Segele, Z. T., Jain, S., Ouma, J. O., Otieno, G., Anyah, R., et al. (2020). Projected effects of 1.5 C and 2 C global warming levels on the intra-seasonal rainfall characteristics over the Greater Horn of Africa. *Environmental Research Letters*, 15(3), 34–37. <https://doi.org/10.1088/1748-9326/ab6b33>
- Hersbach, H., Berrisford, P., Hirahara, S., Horányi, A., Muñoz-Sabater, J., Nicolas, J., et al. (2020). The ERA5 global reanalysis. *Quarterly Journal of the Royal Meteorological Society*, 146(730), 1999–2049. <https://doi.org/10.1002/qj.3803>
- Hoell, A., & Funk, C. (2013a). The ENSO-related West Pacific sea surface temperature gradient. *Journal of Climate*, 26(23), 9545–9562. <https://doi.org/10.1175/jcli-d-12-00344.1>
- Hoell, A., & Funk, C. (2013b). Indo-Pacific sea surface temperature influences on failed consecutive rainy seasons over eastern Africa. *Climate Dynamics*, 43(5–6), 1645–1660. <https://doi.org/10.1007/s00382-013-1991-6>
- Huang, B., Banzon, V. F., Boyer, T., Chepurin, G., Lawrimore, J. H., Menne, M. J., et al. (2017). Extended reconstructed sea surface temperature, version 5 (ERSSTv5): Upgrades, validations, and intercomparisons. *Journal of Climate*, 30(20), 8179–8205. <https://doi.org/10.1175/jcli-d-16-0836.1>
- Husak, G. J., Michaelsen, J., & Funk, C. (2007). Use of the gamma distribution to represent monthly rainfall in Africa for drought monitoring applications. *International Journal of Climatology*, 27(7), 935–944. <https://doi.org/10.1002/joc.1441>

- ICPAC, FEWS-NET, WMO, FAO, WFP, and JRC. (2022a). *Immediate global action required to prevent Famine in the Horn of Africa*. Multi-agency Drought Alert, ICPAC, CHC, FEWS NET, WMO, OCHA, IPC, FCA, FAO, UNHCR, WFP, WHO, UNICEF, UNHCR, World Vision, Mercy Corps, Islamic Relief.
- ICPAC, FEWS-NET, WMO, FAO, WFP, and JRC. (2022b). *Unprecedented drought brings threat of starvation to millions in Ethiopia, Kenya, and Somalia*. Multi-Agency Drought Alert, F. E. W. S. Network, Ed., IGAD Climate Predictions and Applications Centre.
- Indeje, M., Semazzi, F. H., & Ogallo, L. J. (2000). ENSO signals in East African rainfall seasons. *International Journal of Climatology: A Journal of the Royal Meteorological Society*, 20(1), 19–46. [https://doi.org/10.1002/\(sici\)1097-0088\(200001\)20:1<19::aid-joc449>3.0.co;2-0](https://doi.org/10.1002/(sici)1097-0088(200001)20:1<19::aid-joc449>3.0.co;2-0)
- Johnson, N. C. (2013). How many ENSO flavors can we distinguish? *Journal of Climate*, 26(13), 4816–4827. <https://doi.org/10.1175/jcli-d-12-00649.1>
- Kilavi, M., Ambani, M., Robbins, J., Dankers, R., Graham, R., Helen, T., et al. (2018). Extreme rainfall and flooding over central Kenya including Nairobi city during the long-rains season 2018: Causes, predictability, and potential for early warning and actions. *Atmosphere*, 9, 472. <https://doi.org/10.3390/atmos9120472>
- Kirtman, B. P., Infanti, J. M., Kinter, J. L., Paolino, D. A., Zhang, Q., Van den Dool, H., et al. (2014). The North American Multimodel Ensemble: Phase-1 seasonal-to-interannual prediction; phase-2 toward developing intraseasonal prediction. *Bulletin of American Meteorological Society*, 95(4), 585–601. <https://doi.org/10.1175/bams-d-12-00050.1>
- Korecha, D., & Barnston, A. G. (2007). Predictability of June–September rainfall in Ethiopia. *Monthly Weather Review*, 135(2), 628–650. <https://doi.org/10.1175/mwr3304.1>
- Levin, N. E., Zipser, E. J., & Cerling, T. E. (2009). Isotopic composition of waters from Ethiopia and Kenya: Insights into moisture sources for eastern Africa. *Journal of Geophysical Research*, 114(D23). <https://doi.org/10.1029/2009jd012166>
- L'Heureux, M. L., Lee, S., & Lyon, B. (2013). Recent multidecadal strengthening of the Walker circulation across the tropical Pacific. *Nature Climate Change*, 3(6), 571–576. <https://doi.org/10.1038/nclimate1840>
- Liebmann, B., Funk, C., Bladé, I., Dole, R. M., Allured, D., Quan, X., et al. (2014). Understanding recent eastern Horn of Africa rainfall variability and change. *Journal of Climate*, 27(23), 8630–8645. <https://doi.org/10.1175/jcli-d-13-00714.1>
- Liebmann, B., Funk, C., Bladé, I., Dole, R. M., Allured, D., Quan, X., et al. (2020). Biases in CMIP5 sea surface temperature and the annual cycle of East African rainfall. *Journal of Climate*, 33(19), 8209–8223. <https://doi.org/10.1175/jcli-d-20-0092.1>
- Liebmann, B., Funk, C., Bladé, I., Dole, R. M., Allured, D., Quan, X., et al. (2021). Biases in sea surface temperature and the annual cycle of Greater Horn of Africa rainfall in CMIP6. *International Journal of Climatology*.
- Liebmann, B., Kiladis, G. N., Carvalho, L. M. V., B. Senay, G., Allured, D., Leroux, S., & Funk, C. (2012). Seasonality of African precipitation from 1996 to 2009. *Journal of Climate*, 25(12), 4304–4322. <https://doi.org/10.1175/jcli-d-11-00157.1>
- Lyon, B. (2014). Seasonal drought in the greater Horn of Africa and its recent increase during the March–May long rains. *Journal of Climate*, 27(21), 7953–7975. <https://doi.org/10.1175/jcli-d-13-00459.1>
- Lyon, B., Barnston, A. G., & DeWitt, D. G. (2013). Tropical pacific forcing of a 1998–1999 climate shift: Observational analysis and climate model results for the boreal spring season. *Climate Dynamics*, 43(3–4), 893–909. <https://doi.org/10.1007/s00382-013-1891-9>
- Lyon, B., & DeWitt, D. G. (2012). A recent and abrupt decline in the East African long rains. *Geophysical Research Letters*, 39(2). <https://doi.org/10.1029/2011gl050337>
- Lyon, B., & Vigaud, N. (2017). Unraveling East Africa's climate paradox. *Climate Extremes: Patterns and Mechanisms*, 265, 281.
- MacLeod, D. (2018). Seasonal predictability of onset and cessation of the east African rains. *Weather and Climate Extremes*, 21, 27–35. <https://doi.org/10.1016/j.wace.2018.05.003>
- MacLeod, D., Graham, R., O'Reilly, C., Otieno, G., & Todd, M. (2021). Causal pathways linking different flavours of ENSO with the Greater Horn of Africa short rains. *Atmospheric Science Letters*, 22(2), e1015. <https://doi.org/10.1002/asl.1015>
- Mantua, N., & Hare, S. (2002). The pacific decadal oscillation. *Journal of Oceanography*, 58(1), 35–44. <https://doi.org/10.1023/a:1015820616384>
- Maybee, B., Ward, N., Hirons, L. C., & Marsham, J. H. (2022). Importance of Madden–Julian oscillation phase to the interannual variability of East African rainfall. *Atmospheric Science Letters*, 24(5), e1148. <https://doi.org/10.1002/asl.1148>
- Meinshausen, M., Lewis, J., Gidden, M. J., Vogel, E., Freund, M., Beyerle, U., et al. (2020). The shared socio-economic pathway (SSP) greenhouse gas concentrations and their extensions to 2500. *Geoscientific Model Development*, 13, 3571–3605. <https://doi.org/10.5194/gmd-13-3571-2020>
- Nicholson, S. E. (2014). A detailed look at the recent drought situation in the Greater Horn of Africa. *Journal of Arid Environments*, 103, 71–79. <https://doi.org/10.1016/j.jaridenv.2013.12.003>
- Nicholson, S. E. (2015). Long-term variability of the East African 'short rains' and its links to large-scale factors. *International Journal of Climatology*, 35(13), 3979–3990. <https://doi.org/10.1002/joc.4259>
- Nicholson, S. E. (2016). An analysis of recent rainfall conditions in eastern Africa. *International Journal of Climatology*, 36(1), 526–532. <https://doi.org/10.1002/joc.4358>
- Nicholson, S. E. (2017). Climate and climatic variability of rainfall over eastern Africa. *Reviews of Geophysics*, 55(3), 590–635. <https://doi.org/10.1002/2016rg000544>
- NOAA. (2022). *Cold & warm episodes by season*. Retrieved from [https://origin.cpc.ncep.noaa.gov/products/analysis\\_monitoring/ensostuff/ONI\\_v5.php](https://origin.cpc.ncep.noaa.gov/products/analysis_monitoring/ensostuff/ONI_v5.php)
- Ogallo, L. J., Janowiak, J. E., & Halpert, M. S. (1988). Teleconnection between seasonal rainfall over East Africa and global sea surface temperature anomalies. *Journal of the Meteorological Society of Japan*, 66(6), 807–822. <https://doi.org/10.2151/jmsj1965.66.6.807>
- Ogega, O. M., Koske, J., Kung'u, J. B., Scoccimarro, E., Endris, H. S., & Mistry, M. N. (2020). Heavy precipitation events over East Africa in a changing climate: Results from CORDEX RCMs. *Climate Dynamics*, 55(3–4), 993–1009. <https://doi.org/10.1007/s00382-020-05309-z>
- Park, S., Kang, D., Yoo, C., Im, J., & Lee, M.-I. (2020). Recent ENSO influence on East African drought during rainy seasons through the synergistic use of satellite and reanalysis data. *ISPRS Journal of Photogrammetry and Remote Sensing*, 162, 17–26. <https://doi.org/10.1016/j.isprsjprs.2020.02.003>
- Peixoto, J. P., Oort, A. H., Covey, C., & Taylor, K. (1992). Physics of climate. *American Institute of Physics*, 45(8), 67. <https://doi.org/10.1063/1.2809772>
- Pohl, B., & Camberlin, P. (2006). Influence of the Madden–Julian oscillation on East African rainfall: II. March–May season extremes and interannual variability. *Quarterly Journal of the Royal Meteorological Society*, 132(621), 2541–2558. <https://doi.org/10.1256/qj.05.223>
- Rowell, D. P., Booth, B. B. B., Nicholson, S. E., & Good, P. (2015). Reconciling past and future rainfall trends over East Africa. *Journal of Climate*, 28(24), 9768–9788. <https://doi.org/10.1175/jcli-d-15-0140.1>
- Roxy, M. K., Dasgupta, P., McPhaden, M. J., Suematsu, T., Zhang, C., & Kim, D. (2019). Twofold expansion of the Indo-Pacific warm pool warps the MJO life cycle. *Nature*, 575(7784), 647–651. <https://doi.org/10.1038/s41586-019-1764-4>
- Rubiano, M. P. (2022). *How scientists predict famine before it hits*. BBC Future Planet, British Broadcasting Company.

- Schwarzwalder, K., Goddard, L., Seager, R., Ting, M., & Marvel, K. (2022). Understanding CMIP6 biases in the representation of the greater Horn of Africa long and short rains.
- Seager, R., Cane, M., Henderson, N., Lee, D.-E., Abernathy, R., & Zhang, H. (2019). Strengthening tropical Pacific zonal sea surface temperature gradient consistent with rising greenhouse gases. *Nature Climate Change*, 9(7), 517–522. <https://doi.org/10.1038/s41558-019-0505-x>
- Seager, R., Henderson, N., & Cane, M. (2022). Persistent discrepancies between observed and modeled trends in the tropical Pacific Ocean. *Journal of Climate*, 35(14), 1–41. <https://doi.org/10.1175/jcli-d-21-0648.1>
- Shukla, S., Husak, G., Turner, W., Davenport, F., Funk, C., Harrison, L., & Krell, N. (2021). A slow rainy season onset is a reliable harbinger of drought in most food insecure regions in Sub-Saharan Africa. *PLoS One*, 16(1), e0242883. <https://doi.org/10.1371/journal.pone.0242883>
- Shukla, S., Roberts, J., Hoell, A., Funk, C. C., Robertson, F., & Kirtman, B. (2016). Assessing North American multimodel ensemble (NMME) seasonal forecast skill to assist in the early warning of anomalous hydrometeorological events over East Africa. *Climate Dynamics*, 53(12), 1–17. <https://doi.org/10.1007/s00382-016-3296-z>
- Tierney, J., Smerdon, J., Anchukaitis, K., & Seager, R. (2013). Multidecadal variability in East African hydroclimate controlled by the Indian ocean. *Nature*, 493(7432), 389–392. <https://doi.org/10.1038/nature11785>
- Tierney, J. E., Ummenhofer, C. C., & deMenocal, P. B. (2015). Past and future rainfall in the Horn of Africa. *Science Advances*, 1(9), 1–8. <https://doi.org/10.1126/sciadv.1500682>
- Trenberth, K. E., & Stepaniak, D. P. (2003a). Covariability of components of poleward atmospheric energy transports on seasonal and interannual timescales. *Journal of Climate*, 16(22), 3691–3705. [https://doi.org/10.1175/1520-0442\(2003\)016<3691:cocopa>2.0.co;2](https://doi.org/10.1175/1520-0442(2003)016<3691:cocopa>2.0.co;2)
- Trenberth, K. E., & Stepaniak, D. P. (2003b). Seamless poleward atmospheric energy transports and implications for the Hadley circulation. *Journal of Climate*, 16(22), 3706–3722. [https://doi.org/10.1175/1520-0442\(2003\)016<3706:spaeta>2.0.co;2](https://doi.org/10.1175/1520-0442(2003)016<3706:spaeta>2.0.co;2)
- Verdin, J., Funk, C., Senay, G., & Choularton, R. (2005). Climate science and famine early warning. *Philosophy of Transactions Royal Society B*, 360(1463), 2155–2168. <https://doi.org/10.1098/rstb.2005.1754>
- Viste, E., & Sorteberg, A. (2013). Moisture transport into the Ethiopian highlands. *International Journal of Climatology*, 33(1), 249–263. <https://doi.org/10.1002/joc.3409>
- Voosen, P. (2020). The hunger forecast. *Science*, 368(6488), 226–229. <https://doi.org/10.1126/science.368.6488.226>
- Wainwright, C. M., Marsham, J. H., Keane, R. J., Rowell, D. P., Finney, D. L., Black, E., & Allan, R. P. (2019). 'Eastern African Paradox' rainfall decline due to shorter not less intense Long Rains. *npj Climate and Atmospheric Science*, 2, 1–9. <https://doi.org/10.1038/s41612-019-0091-7>
- Walker, D. P., Marsham, J. H., Birch, C. E., Scaife, A. A., & Finney, D. L. (2020). Common mechanism for interannual and decadal variability in the East African long rains. *Geophysical Research Letters*, 47(22), e2020GL089182. <https://doi.org/10.1029/2020gl089182>
- Wheeler, M. C., & Hendon, H. H. (2004). An all-season real-time multivariate MJO index: Development of an index for monitoring and prediction. *Monthly Weather Review*, 132(8), 1917–1932. [https://doi.org/10.1175/1520-0493\(2004\)132<1917:aarmmi>2.0.co;2](https://doi.org/10.1175/1520-0493(2004)132<1917:aarmmi>2.0.co;2)
- Williams, P., & Funk, C. (2011). A westward extension of the warm pool leads to a westward extension of the Walker circulation, drying eastern Africa. *Climate Dynamics*, 37(11–12), 2417–2435. <https://doi.org/10.1007/s00382-010-0984-y>
- Wills, R. C. J., Dong, Y., Proistosescu, C., Armour, K. C., & Battisti, D. S. (2022). Systematic climate model biases in the large-scale patterns of recent sea-surface temperature and sea-level pressure change. *Geophysical Research Letters*, 49(17), e2022GL100011. <https://doi.org/10.1029/2022gl100011>
- Yang, W., Seager, R., Cane, M. A., & Lyon, B. (2014). The East African long rains in observations and models. *Journal of Climate*, 27(19), 7185–7202. <https://doi.org/10.1175/jcli-d-13-00447.1>
- Zhang, C. (2005). Madden-Julian oscillation. *Reviews of Geophysics*, 43(2). <https://doi.org/10.1029/2004rg000158>